Front. Chem. Sci. Eng. 2021, 15(6): 1462–1486
https://doi.org/10.1007/s11705-021-2099-x

REVIEW ARTICLE

Multifunctional heteroatom zeolites: construction and applications

Qifeng Lei[1], Chang Wang[1], Weili Dai (✉)[1], Guangjun Wu[1], Naijia Guan[1,2], Landong Li[1,2]

1 School of Materials Science and Engineering & National Institute for Advanced Materials, Nankai University, Tianjin 300350, China
2 Key Laboratory of Advanced Energy Materials Chemistry of the Ministry of Education, Nankai University, Tianjin 300071, China

Abstract Multifunctional heteroatom zeolites have drawn broad attentions due to the possible synergistic effects in the catalytic reactions. Remarkable achievements have been made on the synthesis, characterization and catalytic applications of multifunctional heteroatom zeolite, while a review on this important topic is still missing. Herein, current research status of multifunctional heteroatom zeolites is briefly summarized, aiming to boost further researches. First, the synthesis strategies toward heteroatom zeolites are introduced, including the direct synthesis and postsynthesis routes; then, the spectroscopic techniques to identify the existing states of heteroatom sites and the corresponding physiochemical properties are shown and compared; finally, the catalytic applications of multifunctional heteroatom zeolites in various chemical reactions, especially in one-step tandem reactions, are discussed.

Keywords zeolite, multifunctional active sites, heteroatom, characterization, catalysis

1 Introduction

With the advantages of large specific surface areas, abundant pore architectures, remarkable hydrothermal stability and adjustable acidity, zeolites have been widely utilized as catalysts in many chemical reactions. The introduction of heteroatoms into the zeolite framework is one of the important strategies for the modifications of zeolites to improve their catalytic performance and broaden their catalytic applications. After the introduction of heteroatoms, the zeolite framework structure can be well preserved, while the physiochemical properties, e.g., acidity and redox properties, can be modulated, thereby changing their catalytic behaviors.

Since Taramasso et al. [1] first implanted heteroatom Ti into the framework of the MFI zeolite (TS-1, titanium silicalite-1) in 1983, the conventional acid-base catalysis by zeolites has been extended to oxidation-reduction catalysis. The unique three-dimensional ten-membered ring channels of TS-1 zeolite provides unique shape selective catalysis in a series of oxidation reactions utilizing H_2O_2 as the oxidant, while they are not suitable for macromolecular substrate owing to the small pore windows of ca. 0.55 nm. Therefore, a variety of heteroatom zeolites with larger pore sizes have been developed, such as TS-2 [2], Ti-Beta [3], etc. Recently, with the continuous development of petrochemicals and fine chemicals, the efficient utilization of heavy-component oils becomes impending and, therefore, leads to the emergence of heteroatom-containing mesoporous molecular sieves, e.g., Ti-MCM-41 [4], Ti-MCM-48 [5] and Ti-MSU [6]. The heteroatoms successfully introduced into the zeolite framework can be divided into three categories: main group atoms (Al [7], B [8], Ge [9], Ga [10] and Sn [11], etc.), transition metals (Cr [12], Ni [13], Fe [14], Nb [15], Y [16], etc.) and rare earth metals (La [17], Ce [18], etc.). On the basis of the pore size, the molecular sieves can be divided into four types: small microporous (CHA, KFI and LTA), medium microporous (such as MFI and FER), large microporous (such as FAU and BEA), and mesoporous (such as MCM-41 and SBA-15) molecular sieves [19–22]. Although significant achievements have been made in the synthesis and applications of heteroatom zeolites, most of them are focused on the heteroatom zeolites with a single metal component [23], while the construction and catalytic applications of multifunctional heteroatom zeolites containing two or more framework metals (Al, Ti, Sn, Zr, etc.) are still missing.

Ti and/or Sn- containing heteroatom zeolites are widely investigated in the liquid phase selective oxidation

Received May 10, 2021; accepted July 19, 2021

E-mail: weilidai@nankai.edu.cn

reactions. The Ti-zeolite/H_2O_2 system has shown great advantages in the olefin epoxidation and ketone ammoximation, which are now successfully applied in industrial plants. Sn-containing zeolites have potential prospects for applications in biomass conversion due to the unique Lewis acidic properties. Although the heteroatom zeolites with a single metal component can exhibit the remarkable catalytic performance in a specific reaction, they cannot meet the requirements for more complicated catalytic reactions, such as multi-step tandem or cascade reactions. Consequently, constructing multifunctional heteroatom zeolite catalysts is essential for the multi-step tandem reaction. Remarkable achievements have been made concerning the construction and catalytic applications of multifunctional heteroatom zeolites, while the corresponding review is still missing and therefore, is the main aim of the present article. Herein, the most representative progresses in heteroatom zeolites are briefly summarized, aiming to boost the further researches timely. The synthesis strategies toward heteroatom zeolites, the spectroscopic techniques to determine the active sites and their catalytic applications are included. On the basis of the present research status, the perspective and outlook about the future development of multifunctional heteroatom zeolites are shown.

2 Synthesis strategies for heteroatom zeolites

In general, heteroatom zeolites can be synthesized by two strategies, i.e., the direct synthesis and post-synthesis (Table 1).

2.1 Direct synthesis strategy

In the direct synthesis procedure, heteroatoms are introduced into zeolites utilizing the metalorganics or metal salt solutions as the metal precursors. For hydrothermal synthesis, the metal heteroatom solutions are added into silica alumina sol to generate silica alumina and heteroatom acid salt sols, guaranteeing the homogeneous dispersion of the heteroatoms. Inspired by the successful synthesis of TS-1 by ENI Company via the hydrothermal procedure [1], Ti-containing zeolites with other topologies, e.g., Ti-BEA, Ti-CHA and Ti-MWW, have also been directly synthesized using various organic structure-directing agents [60–64], and the corresponding procedures have been reviewed by Moliner and Corma [65]. Additionally, Corma et al. [66–69] have synthesized Sn-BEA, Nb-BEA and Ta-BEA zeolites as the robust Lewis acidic zeolite catalysts.

When Al and heteroatom metal sources are simultaneously added into the hydrothermal synthesis system, the bifunctional Brønsted-Lewis acidic zeolite catalyst can be obtained. Meng et al. successfully synthesized bifunctional Brønsted-Lewis acidic [Al,Zr]-FAU zeolite by simultaneously adding $Al_2(SO_4)_3$ and $ZrSO_4$ under hydrothermal conditions without organic templates [24]. In comparison with traditional FAU zeolite (USY), [Al,Zr]-Y showed higher catalytic activity in the cracking of 1,3,5-triisopropylbenzene. Bai et al. prepared bifunctional Sn-Al-MFI zeolite by hydrothermal synthesis using diquaternary ammonium ($[C_{22}H_{45}\text{-}N^+(CH_3)_2\text{-}C_6H_{12}\text{-}N^+(CH_3)_2\text{-}C_6H_{13}]Br^{2-}$) as template [25]. The obtained bifunctional zeolite with layered mesopore and micropore structure exhibited remarkable activity in the reaction of glucose to

Table 1 The synthesis and application of multifunctional heteroatom zeolites

Synthesis strategy	Multifunctional heteroatom zeolites	Selected applications	Refs.
Hydrothermal synthesis	[Al,Zr]-Y	1,3,5-Triisopropylbenzene cracking	[24]
	Sn-Al-MFI, Al-Sn-Beta, Zr-Al-TUD-1	Biomass conversion	[25–27]
	Ga-Fe-MFI	Methanol to olefin	[28]
	W-MFI, Sn-MFI	Separation and detection of CO_2 and NO_x	[29,30]
	CrCoAPO-5, FeCoMnAPO-5	Cyclohexane oxidation	[31,32]
	W-TS-1	Oxidative desulfurization	[33]
	H-GaAlMFI	Methane oxidation	[34]
Post synthesis	Sn-Al-zeolite, Zr-Al-zeolite, Sn-β-Ca, In-Sn-Beta, Zn-Sn-Beta, Mg-Sn-Beta	Biomass conversion	[35–48]
	Ag/ZrBEA, CuTaSiBEA, ZnHf-MFI	Ethanol to butadiene	[49–51]
	PtSn-Beta, Pt/Sn-Beta, PtSn/TS-1	Propane dehydrogenation	[52–54]
	Pd/Ti-MCM-41, TiSn-Beta	Olefin epoxidation	[55,56]
	Ir/Fe-USY (ultrastable Y zeolite)	N_2O decomposition	[57]
	CuMn-HBeta	Soot oxidation	[58]
	SnAl-Beta	Polyoxymethylene dimethyl ethers synthesis	[59]

5-(ethoxymethyl)furfural. Jin et al. prepared multifunctional Ga-Fe-MFI zeolite via the hydrothermal synthesis route [28]. In comparison with the ion-exchange Fe-containing MFI zeolite, the H-FeGaAl-MFI zeolite exhibited higher activity and anti-coking ability in the methanol-to-olefins reaction. On the other side, the co-introduction of Ga species in the MFI framework could obviously enhance the selectivity to light olefins.

In the direct synthesis route, nitrate, acetate and chloride are often utilized as the metal heteroatom sources, but the crystallization process is very long and the number of heteroatoms incorporating into the zeolite framework is limited. Even such a small number of heteroatoms can greatly influence the physiochemical properties and broaden the catalytic applications. In addition, the direct hydrothermal synthesis has a large operation space for optimizing the crystal structure and zeolite morphology by controlling the synthesis conditions. However, the shortcomings of direct synthesis route such as a time-consuming crystallization process, high cost of organic templates, and low content of framework heteroatoms have greatly hindered the large-scale industrial applications.

Similar like hydrothermal synthesis, dry-gel conversion is also used for preparing heteroatom zeolites [70] (Fig. 1), such as Ti- and Sn-containing zeolites. Niphadkar et al. synthesized Sn-MFI zeolites for the first time using the method of steam-assisted dry gel conversion [71]. Typically, the high concentration of the templating agents utilizing in this process could greatly accelerate the nucleation rate of Ti and Sn species, and achieve a 100% crystallinity after crystallization for 53 h. Additionally, the saturated vapor pressure could promote the interaction between the Ti and/or Sn and Si sources, thus accelerating the growth of crystal nucleus and shortening the crystallization time. Through the similar method, Kang et al. successfully prepared a regular-shaped Sn-BEA zeolite within 5 h [72]. In a word, the strategy of dry-gel conversion can greatly shorten the crystallinity time and avoid the extensive use of expensive templates and the generation of strong alkali waste. However, owing to the inhomogeneous mass and heat transfer, this strategy has not yet been applied in industry.

2.2 Post synthesis strategy

Due to the difference in the radii of transition metals and Si/Al ions as well as their mismatching hydrolysis rates during the synthesis, there exist great difficulties and shortcomings in the direct synthesis method, such as the low content of heteroatoms incorporated into the zeolite framework in alkaline synthesis systems, long time required for complete crystallization, easy formation of large crystalline domains and extra-framework heteroatoms [23]. Therefore, the post-synthesis procedures with high heteroatom contents have been developed. The two-step post synthesis strategy consists of the zeolite dealumination and subsequent introduction of metal species into the dealuminated zeolite.

The post-treatment strategy for the synthesis of monometallic heteroatom zeolites includes gas-solid isomorphous substitution [73–75], liquid-solid isomorphous substitution [76–81], and solid-state ion-exchange method [82–84]. The gaseous metal sources utilized in the gas-solid deposition process can accelerate the mass transfer of metal ions and thus facilitate the rapid coordination between the metal ions and the defects of zeolite framework. Ding et al. successfully prepared Ti-MOR zeolite via the gas-solid isomorphous substitution [85]. First, high-silica MOR zeolite was produced via the dealumination of H-MOR in concentrated HNO_3. Subsequently, the dealuminated sample was penetrated by $TiCl_4$ vapor at 400 °C and the Si–OH defects could interact with $TiCl_4$, thus leading the incorporation of Ti species into MOR framework. The impregnation method is a typical approach to synthesize supported heteroatom zeolites via the post-synthesis route. Sn-BEA zeolite was obtained with Sn content of only 0.4% after placing the dealuminated Beta and $SnCl_4 \cdot 5H_2O$ in isopropanol solution for backflow in 7 h [76]. The isopropanol solvent at the outskirts of tin ions could form a shell structure, thus increasing the diffusion resistance of tin species into the zeolite framework and resulting in the low contents of framework tin species. Dzwigaijs et al. [77–81] also prepared V-BEA, Ta-BEA, Nb-BEA, Ti-BEA and Fe-BEA heteroatom zeolites via the liquid-solid isomorphous substitution method. Recently,

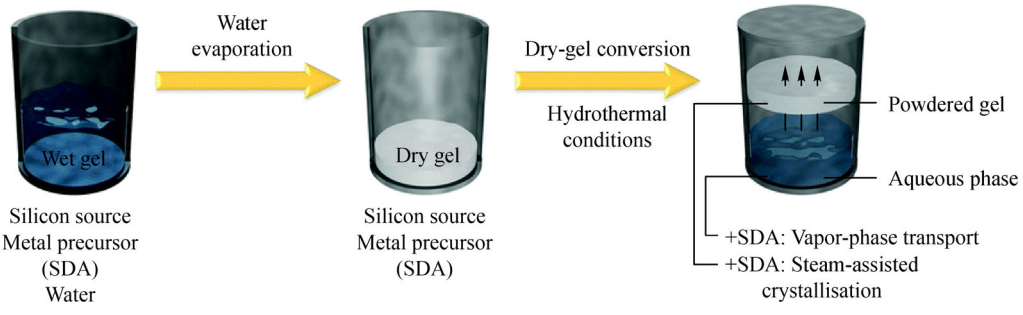

Fig. 1 Procedure for the synthesis of tin-containing zeolites by dry-gel conversion. Reprinted with permission from ref. [70], copyright 2015, Royal Society of Chemistry.

solid-state ion-exchange method is widely utilized for preparing heteroatom zeolites. Directly mixing the solid metal source with the dealuminated zeolite with completely grinding can contribute to improving the mass transfer capacity of the metal source and avoiding the self-aggregation. Recently, Sn-BEA, Ce-BEA and Zr-BEA zeolites were successfully prepared via the solid-state ion-exchange method using $Sn(CH_3)_2Cl_2$, $Ce(OC_3H_7)_4$, $Zr(CP)_2Cl_2$ as organometallic precursors, respectively [82–84].

If the Al atoms in zeolite framework are completely removed, Lewis acid sites will be solely formed after the post synthesis procedures. However, when the samples are partially dealuminated, bifunctional zeolites possessing Brønsted and Lewis acid sites can be obtained via the post-treatment strategy. Dijkmans et al. prepared the bifunctional Sn-Al-BEA zeolite with both Brønsted (Al sites) and Lewis (Sn sites) acid sites via the post synthesis method [35]. Beta zeolite was partially dealuminated by acidic treatment with HNO_3 (the HNO_3 concentration varying from 1.44 to 14.4 $mol \cdot L^{-1}$, depending on the target degree of Al removal), followed by contact with $SnCl_4 \cdot 5H_2O$ in isopropanol with reflux setup for 7 h. Li et al. also successfully prepared the bifunctional Sn-Al-BEA zeolite via similar method, which exhibited remarkable activity in the one-pot conversion of glucose to 5-hydroxymethylfurfural [36]. Very recently, this method was also expanded to the synthesis of bifunctional Zr-Al-BEA zeolite (Fig. 2), which exhibited higher catalytic activity in the cascade Meerwein-Ponndorf-Verley (MPV) reaction in comparison with Zr-BEA zeolite [37].

Wang et al. synthesized bifunctional Pt/Sn-Si-BEA zeolite via the combination of solid-state ion-exchange and wet impregnation (Fig. 3) [52]. Sn-BEA zeolite was first prepared through a two-step post synthesis strategy, and then followed by introducing Pt species to Sn-BEA zeolite via wet impregnation. The strong interaction between Pt and the framework Sn(IV) species promoted the homogeneous dispersion of Pt species, thus guaranteeing the good catalytic activity and regeneration stability of Pt/Sn-BEA in the reaction of propane dehydrogenation. Yang et al. prepared Mg-Sn-BEA zeolite by wetness impregnation of dealuminated Beta zeolite with $SnCl_4 \cdot 5H_2O$ and $Mg(NO_3)_2 \cdot 6H_2O$ aqueous solutions, followed by drying at 100 °C and calcination at 550 °C for 5 h [38]. During the post synthesis procedures, Sn species could be incorporated into the zeolite framework and generate Lewis acid sites, while partial Mg^{2+} would

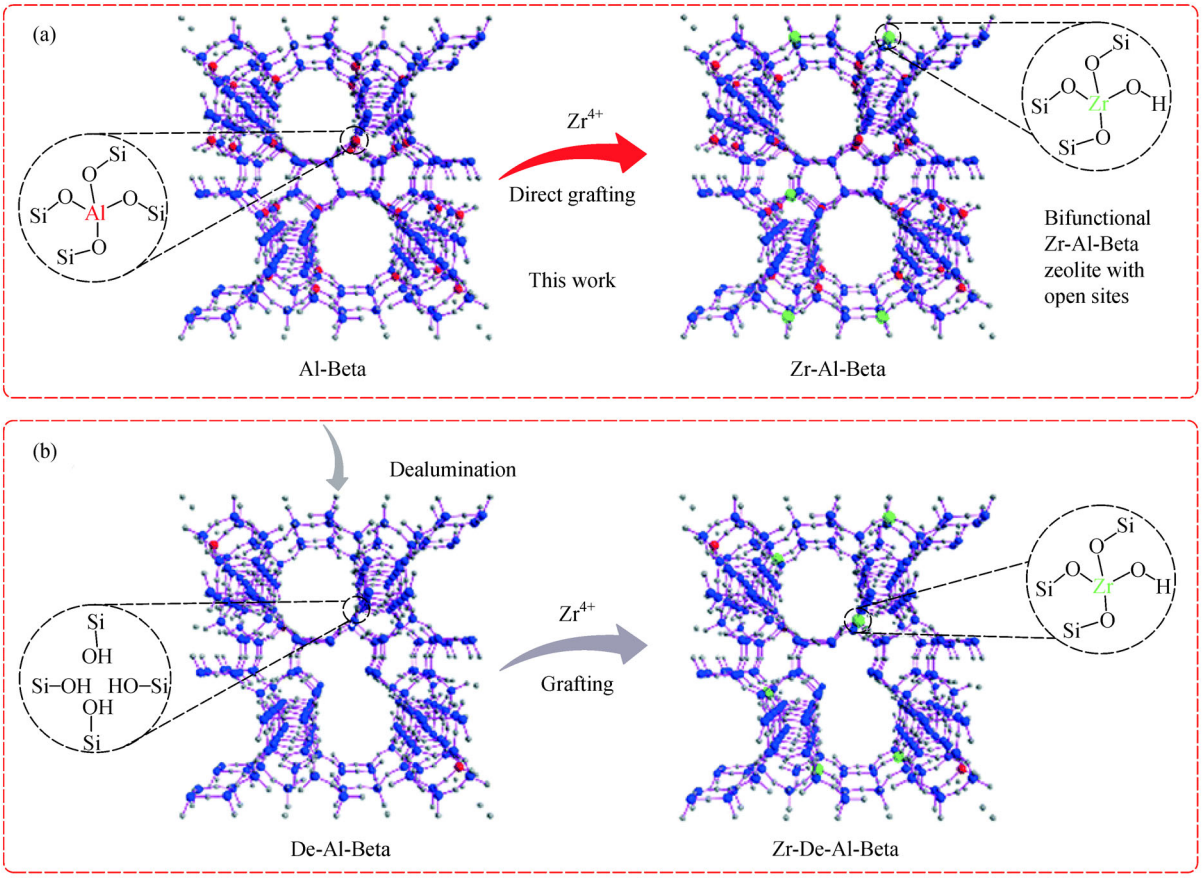

Fig. 2 Schematic synthesis of (a) Zr-Al-BEA and (b) Zr-De-Al-BEA by post-synthesis method. Reprinted with permission from ref. [37], copyright 2019, Royal Society of Chemistry.

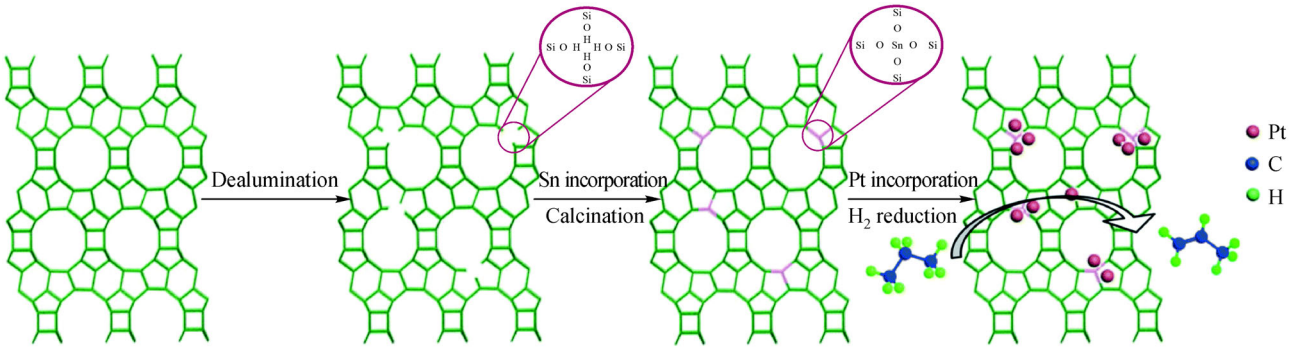

Fig. 3 Illustration of the preparation of the Pt/Sn-Si-BEA catalysts. Reprinted with permission from ref. [52], copyright 2019, Royal Society of Chemistry.

interact with hydroxyl groups of silanol nests and produce extra-framework Mg species. According to balance the Mg/Sn molar ratios, the acidity/basicity of Mg-Sn-BEA zeolites could be well adjusted, thus making them suitable for the glucose to methyl lactate reaction.

Additionally, the post-synthesis strategies can be utilized for the preparation of the heteroatom zeolites like Sn-MOR and Sn-FAU that cannot be easily synthesized via normal hydrothermal route. On the other hand, post-synthesis route has its own shortcomings. First, the framework defects, i.e., silanol nests, randomly generated during the dealumination process, could not be fully eliminated by supplementing heteroatoms, thus leading to poor repeatability; secondly, the heteroatoms are randomly distributed on the zeolite framework, rather than in the thermodynamically stable position, thus leading to relatively low stability in the reaction; finally, a small quantity of extra-framework metal oxides can be formed during the high temperature calcination process.

In summary, it is possible to synthesize zeolites with desired topological structure by controlling the conditions via the direct synthesis route, while it has the limitation in the type and content of the heteroatoms. For the post synthesis strategy, it is suitable for the preparation of heteroatom-containing zeolites that could not be easily synthesized by hydrothermal route or the heteroatom zeolites with high metal content requirements. Therefore, we can rationally choose the strategy to synthesize the multifunctional heteroatom zeolites according to the specific requirements. In addition, the formation of extra-framework metal oxides in the aforementioned two strategies can cover the zeolite surface or block the zeolite pores, making some active sites inaccessible for the reactants. By selecting appropriate ligands and coordination conditions, accurately controlling the rate of hydrolysis and crystallization of the metal source and silicon source in the hydrothermal synthesis system, as well as adjusting the metal source and calcination conditions in the post synthesis route, the formation of non-framework metal species can be effectively suppressed. Additionally, the scale up fabrication of high-quality heteroatom zeolites via the post synthesis procedure is a challenging task. In fact, only a few heteroatom zeolites have been produced in large scale for industrial applications up to now, such as TS-1 zeolite for olefin epoxidation. Therefore, a simple and scalable synthesis strategy with good reproducibility is mostly desired.

3 Characterization of heteroatom zeolites

Reliable characterization approaches are essential to confirm the successful synthesis of heteroatom zeolites. On the basis of characterization and catalytic results, the structure-activity relationship can be established, which is most helpful to guide the design and optimization of multifunctional heteroatom zeolites. In this section, we will summarize the frequently used techniques for the characterization of heteroatom zeolites.

For the multifunctional heteroatom zeolites, it is a hard task to determine the accurate active sites and the interaction between the active sites, and there is no single technique to characterize multi-functional sites simultaneously. Therefore, a combination of various characterization techniques is frequently used to determine the active sites separately, but which is vital to obtain the accurate and comprehensive information on the active sites in multifunctional heteroatom zeolites. Herein, we aim to show the structural and acidic characterization of the heteroatom zeolite by parallel techniques. X-ray diffraction (XRD), Fourier transform infrared spectroscopy (FTIR), Raman spectroscopy, ultraviolet-visible spectroscopy (UV-vis), X-ray photoelectron spectroscopy (XPS), solid-state nuclear magnetic resonance (ssNMR), X-ray absorption spectroscopy (XAS) are often utilized for identifying the structural information and coordination states of heteroatoms. While the temperature programmed desorption of different probe molecules, FTIR and ssNMR associated with different probe molecules are often utilized for acidity characterization (see Fig. 4).

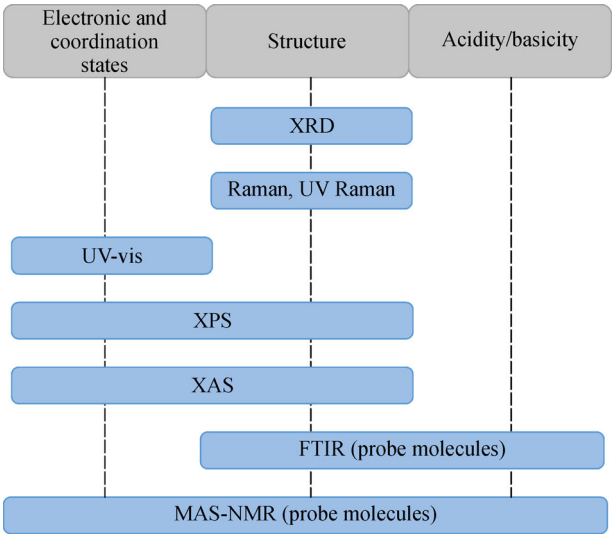

Fig. 4 Characterization techniques used for the heteroatom-containing zeolites and information obtained (UV Raman: UV resonance Raman spectroscopy; MAS-NMR: magic angle spinning NMR).

3.1 XRD

The ion radii of the heteroatoms introduced into the zeolite framework are usually larger than those of the Al, Si, and P atoms in the zeolites. Therefore, the introduction of heteroatom into zeolite framework often causes an increase in the lattice constant and the unit cell volume, which can be detected by a high-precision X-ray powder diffractometer. For example, the introduction of metal species into zeolite framework could cause a slight change of the diffraction peak (302) from $2\theta = 22.68°$ for Si-BEA to $2\theta = 22.50°$ for Ta-Si-BEA, and from $2\theta = 22.63°$ for H-BEA to 22.5° for Ti-BEA [77,86,87]. During the post synthesis procedure, the expansion of the BEA framework would occur after Sn introduction, and the d_{302} spacing gradually increases with enhancing the Sn loadings, e.g., from 3.897Å for Si-BEA (2θ = 22.80°) to 3.927 Å for 5%Sn-BEA and then to 3.939 Å for 10%Sn-BEA [88]. This indirectly demonstrated the expansion of the BEA framework, revealing that Sn species had been successfully introduced into the BEA zeolite framework. In addition, the increase of zeolite unit cell volumes can be observed after heteroatom introduction according to XRD results. In comparison with silicate-1 zeolite, the unit cell volume of Sn-MFI (Si/Sn = 100) zeolite increased from 5.345 to 5.361 nm^3 [89]. In contrast, the extra-framework oxides would not result in the changes of the zeolite unit cell.

3.2 FTIR

FTIR spectroscopy is commonly applied to identify the incorporation of heteroatoms into the zeolite framework according to the difference in the vibration or rotation frequencies of functional groups. Typically, the band at ~960 cm^{-1} is commonly used as an indicator of heteroatom incorporation in the zeolite framework. In addition, the intensities of this band are reported to be proportional to the heteroatom concentration in the zeolite [82,83,90–92]. Therefore, if the heteroatom concentration in the zeolite is very low, the aforementioned absorption band is not obvious or might be overlapped by other bands, making it difficult to identify. In addition, the length of the M–O (M as heteroatom) bond becomes longer in comparison with the heteroatom free counterpart, making the infrared (IR) absorption bands shift to lower wavenumbers. For example, the dominant band at 1100 cm^{-1} attributed to the asymmetric stretching of T–O (where T denotes Si, Al or Fe) bond in Fe-free MFI sample shifts to lower frequency of 1083 and 1086 cm^{-1} for Fe-MFI zeolites. This shift indirectly indicates that the substitution of Fe species in the MFI zeolite framework [93].

During the post synthesis procedure, significant changes in the silanol groups of BEA zeolites can be observed during the dealumination and introduction of metal heteroatoms. Therefore, the diffuse reflectance FTIR spectra of hydroxyl groups on the zeolites are utilized to determine zeolite dealumination and heteroatom introduction. For the parent H-BEA zeolite, a dominant band at 3735 cm^{-1} due to Si–OH defects and an obvious band at 3605 cm^{-1} due to bridging hydroxyl group Si–OH–Al can be observed. After dealumination, the 3605 cm^{-1} band disappears, while a new broad band around 3510 cm^{-1} due to the formation of hydroxyl nests appears. The Si–OH defects and the hydroxyl nests are frequently employed as the anchoring sites for heteroatoms, and significant decreases in the intensities of the bands at 3510 and 3735 cm^{-1} occur on the samples upon the introduction of heteroatoms, indicating that the heteroatom interact with the silanols [82–84,88,94]. However, a very recent study indicated that the frequently utilized FTIR spectroscopy to

determine the introduction of Sn species into BEA zeolite framework require explanation of spectral features with more imprecision and ambiguity [88]. As similar changes in FTIR spectra can both be observed over Sn-containing BEA zeolites with the framework and extra-framework Sn species. That is, the framework Sn sites cannot be directly identified solely by this method.

3.3 UV-vis

UV-vis spectroscopy is also frequently utilized for identifying the coordination states of heteroatoms in zeolites, such as Ti- [14], Zr- [15], V- [16], Fe- [17], W [18] and Sn-containing zeolites [19]. It is generally accepted that the heteroatoms in the zeolite framework will give a sharp absorption peak at 200 to 230 nm, owing to the p–d transition of the lone pair of electrons on the 2p orbital of oxygen to the d empty orbital of the adjacent framework heteroatoms. While the extra-framework oxides show a broad absorption peak at 300 to 480 nm. In addition, as an excellent water-tolerant catalyst, the effect of water on the nature of Sn species in Sn-BEA zeolites can be identified by *in situ* UV-vis spectroscopy [88]. Upon hydration, a red-shift of the band at 207 nm owing to tetrahedrally coordinated Sn species toward higher wavelengths with a maximum absorbance at ca. 224 nm occurred for Sn-BEA zeolite. This new band observed at 224 nm after hydration was attributed to the hydrated forms of isolated Sn(IV) species with high coordination numbers like $Sn(O)_x(OH)_y(H_2O)_z$. While the broad band at around 285 nm due to the extra-framework SnO_2 oxide was nearly unaffected upon both hydration and dehydration. Therefore, the successful incorporation of heteroatoms into the zeolite framework can be identified according to this approach.

3.4 Raman spectroscopy and UV Raman

Most metal oxides have a strong light scattering effect in Raman spectroscopy and, therefore, Raman spectroscopy can be used as an auxiliary means to distinguish heteroatom species in the framework or extra-framework positions. According to the principle of resonant Raman, the Raman bands related to specific heteroatom species can be selectively enhanced with appropriate excitation wavelength.

Currently, Raman spectroscopy is not widely used in the zeolite characterization because of the intense fluorescence interference and the resulting poor quality or even uninterpretable of spectra especially when the frequency of the laser excitation source is in the near-ultraviolet and visible regions. The application of UV Raman can shift the excitation light from the visible region to the ultraviolet region, thus effectively reducing the fluorescence interference and producing a better signal-to-noise ratio [95–99]. Interestingly, the utilization of 244 nm excitation light can selectively enhance the Raman bands related to Ti species in the zeolite framework. In comparison with silicalite-1, new bands at 490, 530 and 1125 cm^{-1} attributed to framework Ti species appear on TS-1 with the utilization of 244 nm excitation light. In contrast, the Raman bands due to the extra-framework Ti species (at 144, 390 and 637 cm^{-1}) are hardly affected. Moreover, the utilization of 266 nm excitation light can accurately determine the Ti species in zeolite framework and identify the open-state octahedrally coordinated Ti species with remarkable catalytic performance [91,100,101]. Recently, Zhang et al. studied the evolution of Ti species during the post-treatment of B-containing Ti-MWW (B-Ti-MWW) zeolite by UV Raman and found that acid treatment of as-synthesized B-Ti-MWW not only removed about half of the absolutely dominant non-framework TiO_6 species but also made the other part converted into framework TiO_4 species [102] (Fig. 5). In contrast, acid treatment of calcined B-Ti-MWW made most of the dominant non-framework TiO_6 species being transformed into anatase TiO_2. The B-Ti-MWW synthesized by acid treatment and subsequent calcination showed good catalytic activity of 1-hexene epoxidation, demonstrating that the acid treatment significantly improved the catalytic performance due to the transformation of non-framework TiO_6 to active framework TiO_4. In short, UV Raman can be an effective method to characterize the framework heteroatoms in the zeolites.

3.5 XPS

XPS is frequently used as a qualitative and also a quantitative method to analyze the atoms on the surface of solid samples and determine their valence states over heteroatom zeolites, such as Y- [16], Nb- [79], Ce- [82], Sn- [52,83], Ti- [94], Mn- [103], and Zr-containing zeolites [84]. The XPS results of Mn 2p3/2 can be fitted to three peaks over Mn-MFI zeolite: the peak at 641.34 eV was attributed to tetrahedral coordination Mn(II) species in zeolite framework, while the peak at the binding energy of 642.51 eV was assigned to Mn(III) species in the framework [103]. Due to the strong interaction between Si and Mn in the framework, their binding energy was greater than the binding energy of manganese oxides (MnO/Mn_2O_3). Several recent studies also indicated [83,52] that XPS can be utilized as an auxiliary means to determine the framework and extra-framework Sn species in the Sn-containing zeolite. Different binding energy values of 487.8 and 486.0 eV attributed to Sn 2p3/2 of tetrahedral framework Sn and octahedrally coordinated extra-framework Sn species, respectively, could be observed.

3.6 ssNMR

ssNMR is an effective tool to determine the microchemical environment and the local structure of heteroa-

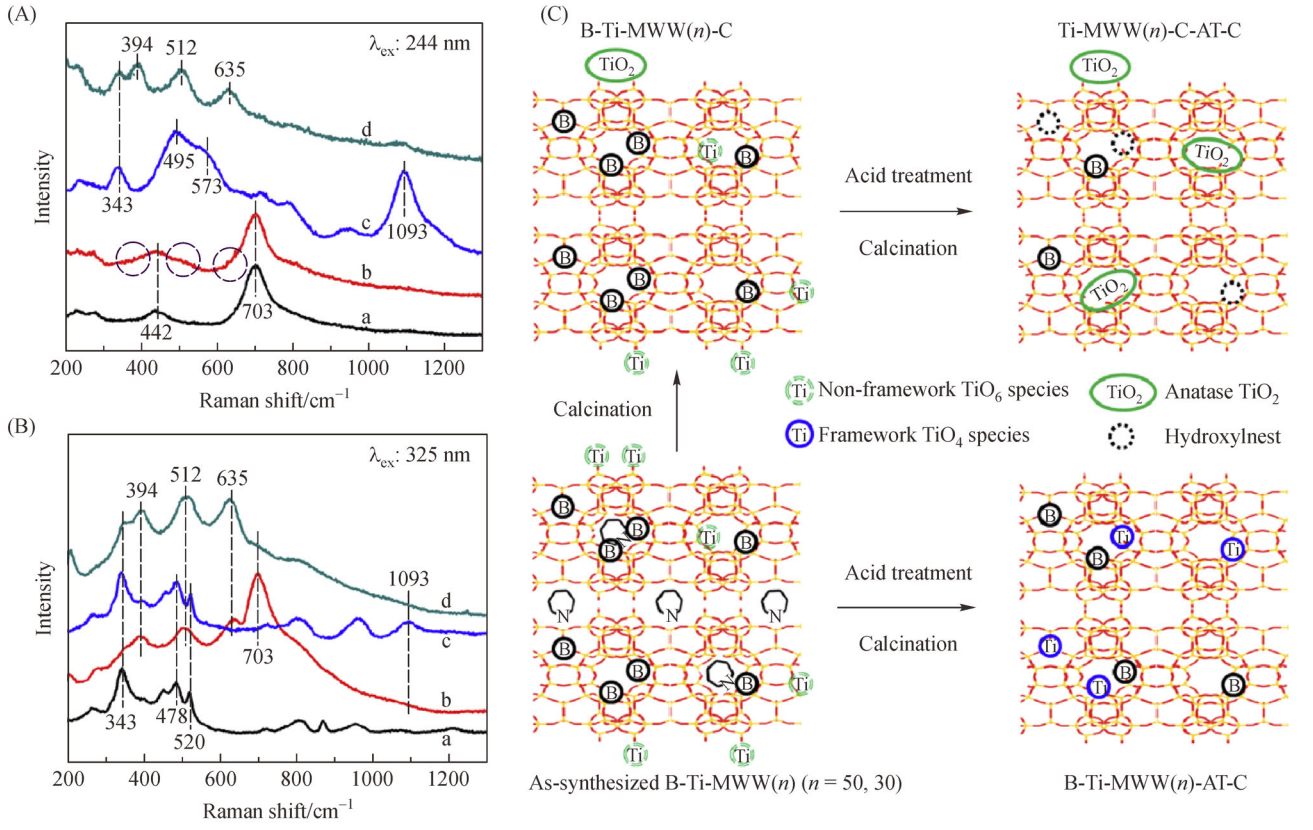

Fig. 5 (A) 244 nm and (B) 325nm excited UV Raman spectra of (a) B-Ti-MWW, (b) B-Ti-MWW-C, (c) B-Ti-MWW-AT-C and (d) B-Ti-MWW-C-AT-C. (C) A possible schematic diagram for the evolution of titanium species in B-Ti-MWW during post-treatments. Reprinted with permission from ref. [102], copyright 2017, Elsevier Inc.

toms in zeolites. It is especially suitable for monitoring tiny changes of zeolite in microstructure using the NMR spectrometer with high magnetic fields. In addition, the crystal structure of the aluminosilicate and silicoaluminophosphate zeolites framework can be directly illustrated by ^{29}Si, ^{27}Al, ^{31}P MAS NMR spectroscopy. ^{29}Si MAS NMR is normally employed to determine the chemical state of framework heteroatoms. Typically, Si–O–M bond formed after the heteroatom (M) incorporating into the framework can lead to the tiny changes in the chemical environment around Si atoms. A new shoulder peak appears at higher magnetic field of the original $Si(OSi)_4$ resonance peak, providing an indirect evidence for the incorporation of heteroatoms into the zeolite framework. For Sn-MFI zeolites [104], the chemical shifts at about –103 and –113 ppm are generally assigned to $Si(OSi)_3(OH)$ (Q^3) and $Si(OSi)_4$ (Q^4), respectively. Typically, the incorporation of Sn atoms into the zeolite framework causes the occurrence of shoulder peaks at around –116 ppm, owing to the induction effect of Sn atom on neighbor Si atoms. Additionally, the ratio of these two peak intensities, I_{-116}/I_{-103}, increased with rising Sn-Si ratio, revealing that the chemical environment around the framework Si changes due to the introduction of Sn species.

While for the heteroatom zeolites, such as B-, Ga- and Sn-containing zeolites, the corresponding ^{11}B, ^{71}Ga and ^{119}Sn MAS NMR spectroscopy can be applied to identify the existing state of heteroatoms. For instance, ^{71}Ga MAS NMR signal at about 156 ppm was assigned to tetrahedral Ga incorporated in zeolite framework, while the signal at around 50 ppm was attributed to extra-framework Ga specie [105,106]. ^{119}Sn MAS NMR spectra is widely utilized to determine the coordination state of Sn species in the Sn-containing zeolite (Fig. 6), and two different coordination states of Sn species in Sn-BEA zeolite framework, i.e., open $Sn(OSi)_3(OH)$ and closed $Sn(OSi)_4$ tetrahedral Sn sites, can be identified. The ^{119}Sn MAS NMR signals at –422 and –443 ppm for dehydrated Sn-zeolite were assigned to open $Sn(OSi)_3(OH)$ and closed $Sn(OSi)_4$ Sn sites, respectively. After hydration, new ^{119}Sn MAS NMR signals at –689 and –703 ppm owing to octahedrally coordinated Sn sites could be observed [107]. Such an interconversion of the tetrahedrally coordinated into octahedrally coordinated Sn sites during the hydration process is related to the coordinated water molecules at Sn sites (Fig. 6(A)). However, the application of this method is limited because of the low natural abundance level of ^{119}Sn isotope (8.6%), which requires an experiment time of several days for each ^{119}Sn MAS NMR measurement [108]. For improving the detection sensitivity on Sn-BEA

zeolites, the dynamic nuclear polarization surface-enhanced NMR spectroscopy (DNP-SENS) was employed, and the sensitivity could be enhanced by 28–75 times (Fig. 6(B)) [108]. Three hexacoordinated Sn species of S1, S2 and S3 could be observed on Sn-BEA zeolite with different Sn content via DNP-SENS NMR technology (Fig. 6(C)) [109]. Further ^{119}Sn two-dimensional cross-polarization magic-angle turning (2D-CPMAT) NMR measurements and theoretical calculations clearly revealed that the S1, S2 and S3 signals of spectra of Sn-BEA were attributed to the six-coordinated "closed" Sn species associated with two water molecules, the six-coordinated "open" tin species with two water molecules and the extra framework SnO_2 species, respectively (Fig. 6(D)). Besides, Deng et al. unambiguously identified the aforementioned two types of open Sn sites via correlating the hydroxyl groups to Sn atoms by one- and two-dimensional proton-detected ^{1}H/^{119}Sn correlation ssNMR spectroscopy (Fig. 6(E)) [110].

3.7 XAS

With the absorption edge as the relative zero point of energy, XAS can be divided into X-ray absorption near

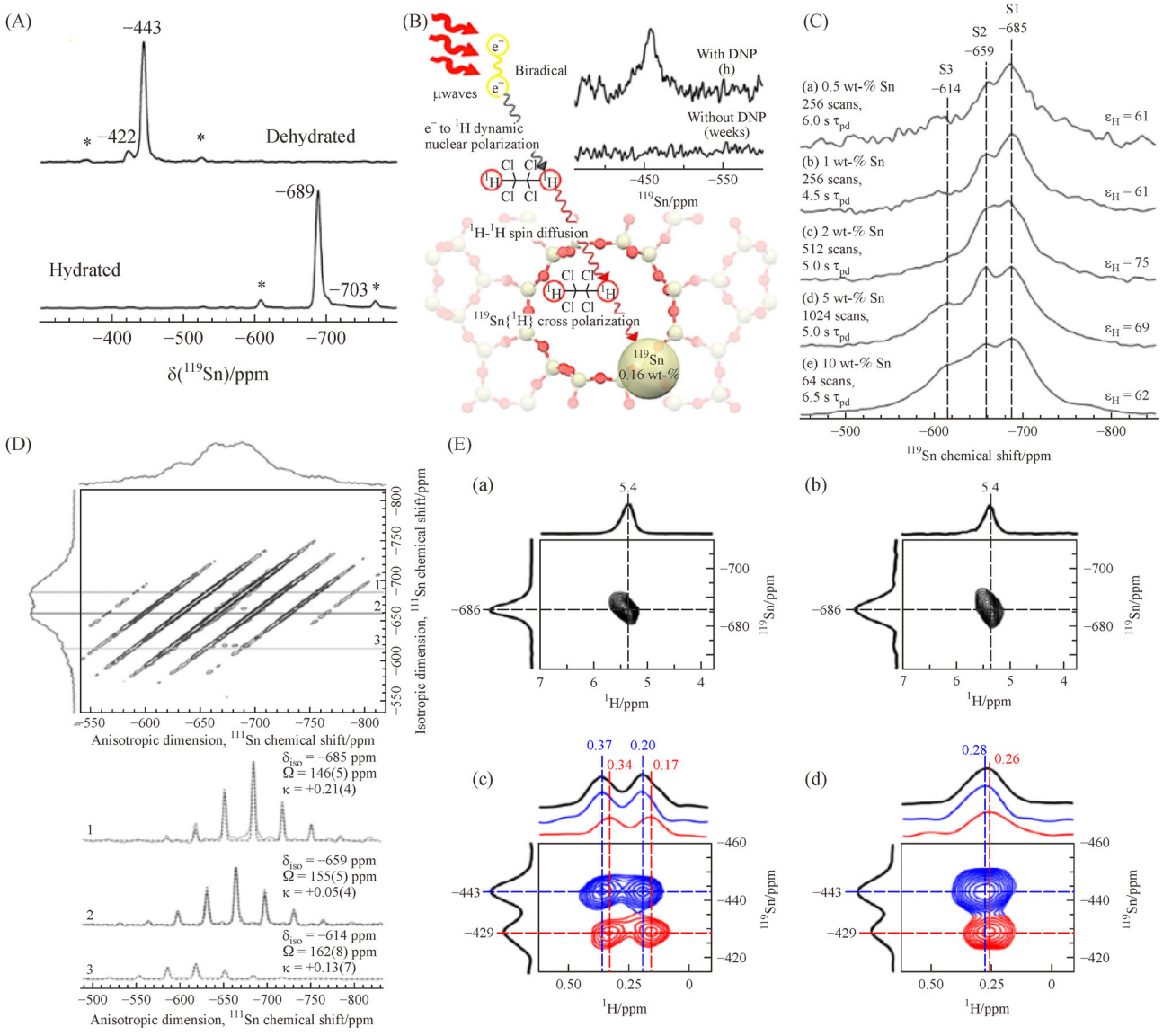

Fig. 6 (A) ^{119}Sn NMR spectra of Sn-BEA. Reprinted with permission from ref. [107], copyright 2019, American Chemical Society. (B) Hyperpolarization of Sn-BEA zeolite using DNP. Reprinted with permission from ref. [108], copyright 2014, American Chemical Society. (C) ^{119}Sn DNP-SENS NMR spectra of various Sn loading Sn-BEA. (D) ^{119}Sn 2D-CPMAT NMR spectra of Sn-BEA. Reprinted with permission from ref. [109], copyright 2014, Wiley-VCH. (E) 2D ^{1}H-^{119}Sn HMQC (heteronuclear multiple quantum correlation) MAS NMR spectra of ^{119}Sn-BEA (a) without dehydration, (b) dehydrated at 298 K, (c) dehydrated at 393 K without ^{119}Sn decoupling, and (d) dehydrated at 393 K with ^{119}Sn decoupling. Reprinted with permission from ref. [110], copyright 2018, Springer Nature.

edge structure (XANES) in the low energy region and extended X-ray absorption fine structure analysis (EXAFS) in the high energy region. The XANES absorption peak is derived from multiple scattering of photoelectrons between adjacent atoms. The shape of the spectrum is associated with the chemical bond type and coordination symmetry of the absorbing atom as well as the electronic transition form of the metal atom. In this way, it is possible to determine the heteroatom species in zeolite framework or extra framework positions. The absorption peaks could be observed in the front edge area of the XANES spectrogram over Fe-MFI, but which are absent over α-Fe_2O_3 and FeOOH (six-coordinated, octahedral geometry) samples. According to the theoretical calculations, the weak absorption peaks were attributed to the 1s–3d electron transition. Based on the dipole transition selection rule, this transition was inhibited in the complete octahedral symmetric structure, whereas it might occur in the tetrahedral coordination structure. Hence, the transition was considered as the transition of Fe in the tetrahedral coordination structure of the zeolite framework [111].

The changes in the photoelectron absorption intensity with the distance from the central atom (the distance represents the number of coordinated layers) demonstrating the short-range order structure state around the absorption atom can also be identified by EXAFS. The first coordination shell of the central atom can be calculated by the single-layer fitting method to obtain important structural information, such as the coordination number and the length of coordination bond. The Sn–O bond length (1.91 Å) of tetrahedrally coordinated framework Sn sites was smaller than the Sn–O bond length (2.05 Å) of the octahedrally coordinated SnO_2 species [112]. Stepanov et al. [113] detected the parameters of Zn^{2+}/H-BEA zeolite: $R_{Zn\text{-}O} \approx 1.96$–$2.02$ Å, CN = 3.8, and $2\sigma^2 = 0.012$ Å^2 via EXAFS spectrogram, without the peak of Zn–O–Zn (in the area of ~2–6 Å), and indicated that the isolated Zn ions were the dominant species in the Zn-containing BEA sample.

Yan et al. [114] found that Co and Ni atoms can be incorporated into MCM-41 structure in the form of octahedral coordination using XANES and EXAFS. The Co atoms in Co-MCM-41 molecular sieve showed the similar pre-edge features as CoO oxides, indicating Co species existed in the form of Co^{2+} in the as-prepared sample. Similar results could also be obtained in the XAS spectra for Ni-MCM-41 sample. Berlier et al. investigated the activation on the Fe states in Fe-MWW zeolite via EXAFS and XANES technique [115]. For the as-synthesized Fe-MWW sample, isolated Fe^{3+} species were presented in tetrahedral coordinated framework with Fe–O distance of 1.87 ± 0.01 Å. Template burning and subsequent activation would cause partial framework Fe^{3+} species migration out of the zeolite framework, accompanied by the reduction of Fe^{3+} to Fe^{2+} (with Fe–O distance of 1.86 ± 0.02 Å). Simultaneously, the XANES characteristic peak (1s → 3d peak of Fe) at 7114.4 eV for Fe^{3+} species shifted a little bit to 7114.3 eV assigned to extra-framework Fe^{2+} species. And the significant reduction of EXAFS signal also showed the reduction of framework iron species, with the Fe–O peak decreasing from 9.7 to 4.3 Å. Partial extra-framework Fe^{2+} species could adsorb NO to form $Fe^{2+}(NO)_3$ complexes, resulting in the corresponding changes in the XANES and EXAFS spectra. This indicates that a mixture of Fe^{2+} and Fe^{3+} ions exist in the calcined Fe-MWW zeolite. That is, Fe species existed in the form of isolated tetrahedral coordinated Fe^{3+} and coordinated unsaturated extra-framework Fe^{2+} species. Lamberti et al. [116] summarized the substitution of Ti, Fe and Ga in zeolite framework by EXAFS and XANES technique. Tetrahedral coordination Ti(IV) species would give an XANES characteristic peak at 4969 eV. In addition, the structural changes of Ti active sites in the TS-1/H_2O_2/H_2O, a good oxidation catalyst system, can be explored by *in situ* XANES and EXAFS spectroscopy (Fig. 7). After the interaction between TS-1 and H_2O_2/H_2O, the XANES pre-edge feature would decrease from 0.9 to 0.16, and two peaks occurred at around 4984 and 4995 eV, owing to the side-on η^2-Ti-peroxo complex. After reaction for 24 h, the aforementioned characteristic peaks almost disappeared because of the water sublimation, but they could be restored by contacting the sample with water again.

3.8 Acidity characterization

After the introduction of heteroatoms, the zeolite structure can be well preserved, while the physiochemical properties, especially the acidity and redox properties, would be greatly altered, thereby influencing the catalytic performance and broadening the catalytic applications. Therefore, the accurate characterization of the acidity of heteroatom zeolite is particularly important for establishing the structure-selectivity relationship.

Temperature programmed desorption of probe molecules is an effective way to analyze the total acid amount and acid strength of zeolite samples [117]. Typically, the basic probe molecules (NH_3, pyridine, *n*-butylamine, quinoline, etc.) are first adsorbed on zeolites. Then, the zeolite samples are treated in inert gas flow or under vacuum to remove the physically adsorbed basic molecules. When NH_3 is utilized as a probe molecule, the desorption temperatures in the NH_3-TPD (temperature-programmed desorption) curve represent the acid strength, while the corresponding peak areas response to the acid density. In addition, IR spectroscopy associated with probe molecules can be utilized as a tool to quantitatively determine the acid type, i.e., Brønsted and Lewis acid sites. Upon pyridine adsorption, the characteristic FTIR peaks appearing at 1540 and 1450 cm^{-1} can be attributed to Brønsted and Lewis acid sites, respectively. In addition, after interacting with pyridine, both Brønsted and Lewis

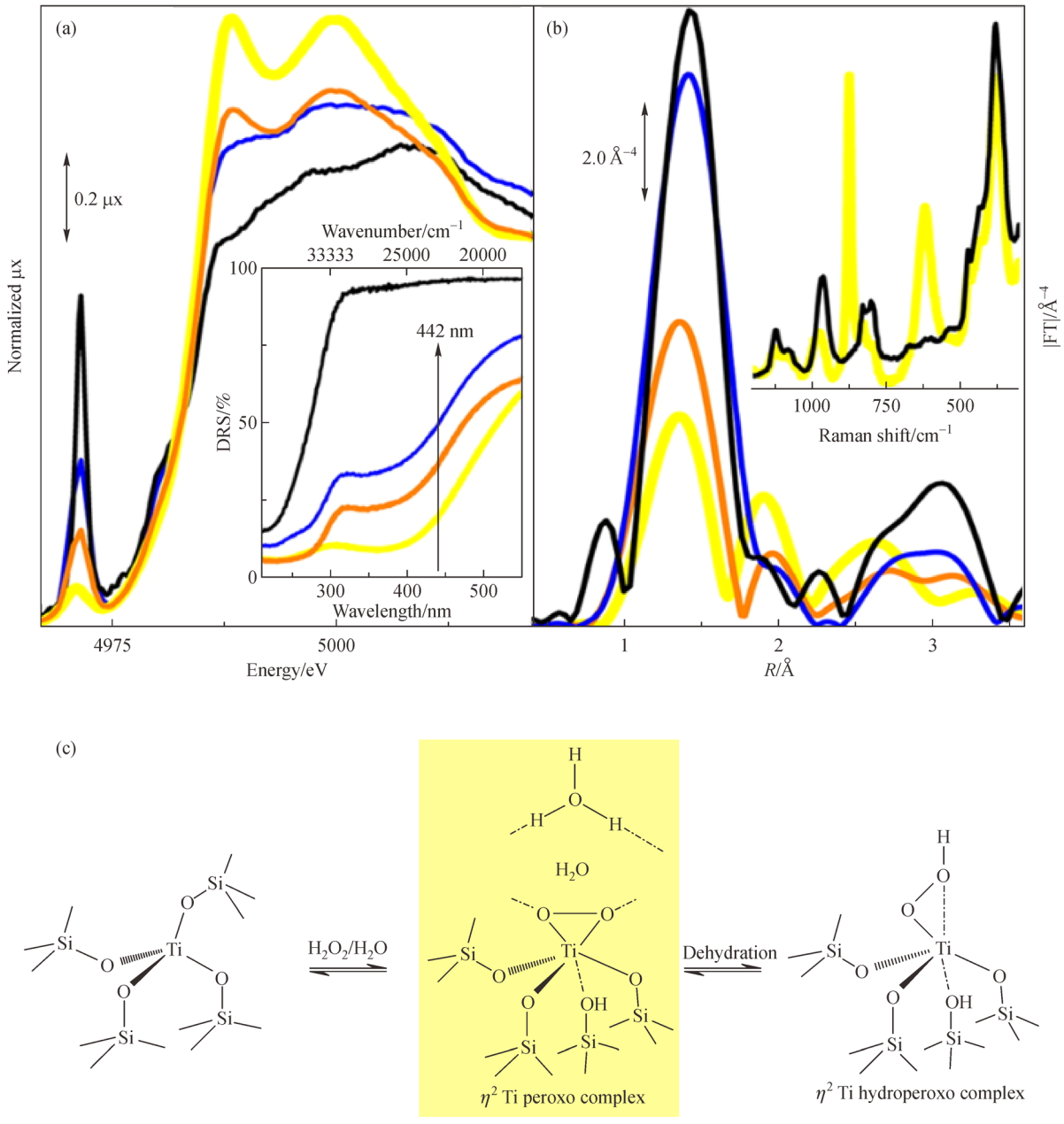

Fig. 7 (a) XANES spectra of TS-1 (black line), after contact with H_2O_2/H_2O solution (yellow line), after time elapse of 24 h (blue line) and subsequent H_2O dosage (orange line); (b) as part a for the k^3-weighted, |FT| of the EXAFS spectra (The insets in parts (a) and (b) report the UV-vis DRS spectra and the Raman spectra); (c) the model hypothesized base on (a) and (b). Reprinted with permission from ref. [116], copyright 2013, American Chemical Society.

acid sites can produce an absorption band at 1490 cm^{-1}. According to the desorption temperature, the acid strength can be compared by this method. For example, TS-1 and Ti-MCM-41 samples with the weak Lewis acid sites both exhibit good catalytic performance in the transesterification reaction [118], but the catalytic activity is in proportion to the acid strength, i.e., TS-1 < Ti-MCM-41. This can be due to the open tetrahedral $Ti(OH)(OSi)_3$ species in Ti-MCM-41 can form a more stable Ti-pyridine complex in comparison with the closed tetrahedral $Ti(OSi)_4$ species in TS-1. Furthermore, associated with FTIR spectroscopy, weakly basic molecules such as pyrrole, CD_3CN, and CO can be applied as probe molecules to determine the surface acidity of the zeolite [49,119–121].

In addition to the aforementioned methods, ssNMR spectroscopy associated with different probe molecules, can be utilized as a powerful means to determine the type, strength and density of acidity in solid acid catalysts (Fig. 8). For example, ^{13}C MAS NMR of adsorbed 2-^{13}C-acetone and ^{1}H MAS NMR of adsorbed NH_3, perdeuterated acetonitrile and pyridine have been utilized to probe

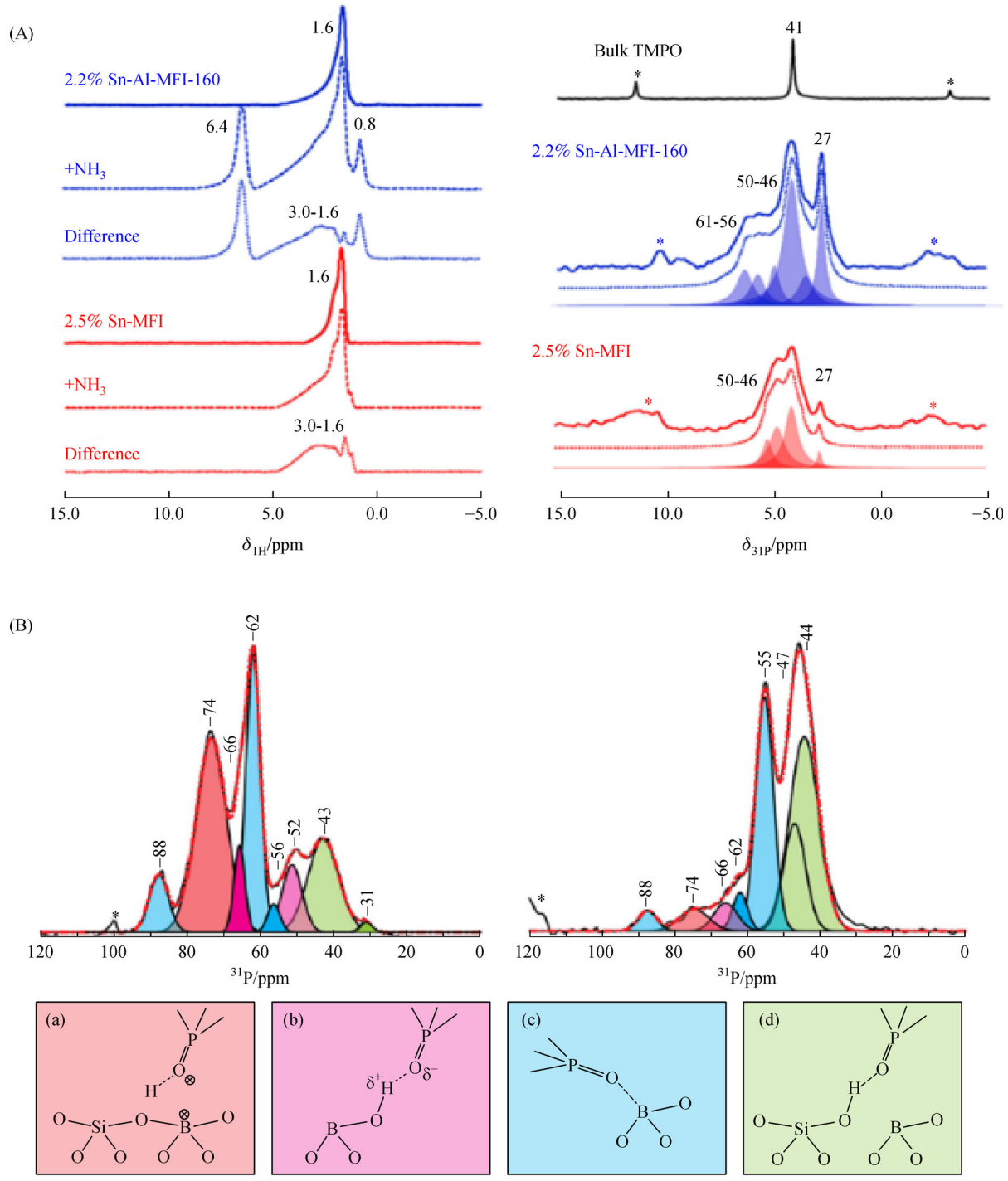

Fig. 8 (A) ^{1}H and ^{31}P MAS NMR spectroscopy of NH_3 and TMPO adsorption on 2.5% Sn-MFI and 2.2% Sn-Al-MFI zeolites. Reprinted with permission from ref. [127], copyright 2018, Elsevier Inc. (B) ^{1}H-decoupled ^{31}P MAS NMR spectrum of TMPO-treated calcined and as-synthesized H-B-MFI, and Schematic sketches of possible interactions between TMPO and Brønsted/Lewis acid sites in H-B-MFI zeolite. Reprinted with permission from ref. [129], copyright 2014, Elsevier Inc.

the acid properties of various solid acids based on acid-base interactions. In particular, ^{31}P MAS NMR of adsorbed phosphorous probe molecules, namely trimethylphosphine (TMP) and trialkylphosphine oxides, have been reported to be sensitive and reliable techniques capable of providing qualitative information such as the type and strength of acid sites in various solid acids [122–126]. In the ^{1}H MAS NMR spectra of NH_3 loaded Sn-MFI and Sn-Al-MFI (Fig. 8(A), left), the signals in the range of δ_{1H} = 0.8–3.0 ppm were attributed to NH_3 adsorbed on Lewis acidic

Sn sites, while the signal at δ_{1H} = 6.4 ppm was assigned to NH_3 adsorbed on Brønsted acid sites. The intensities of aforementioned signals can be utilized for quantifying the number of accessible Lewis and Brønsted acid sites. The acidity of Sn-MFI and Sn-Al-MFI zeolites was also investigated by ^{31}P MAS NMR spectroscopy using TMP oxide (TMPO) as the probe molecule (Fig. 8(A), right) [127]. For Sn-MFI, the ^{31}P MAS NMR signals in the range of 46–50 and 56–61 ppm were attributed to TMPO adsorbed at Lewis acid sites and Brønsted acid sites, respectively. Zhang et al. investigated the relationship between Al distribution and Brønsted acidity of a series of H-BEA zeolites derived from dealumination of Al-rich H-BEA zeolite by ^{27}Al MAS/MQ MAS and ^{31}P MAS NMR spectroscopy using TMPO as probe molecules [128]. Three types of Brønsted acid sites corresponding to different specific Al T-sites were demonstrated. Mafra et al. investigated the acid properties of a dehydrated borosilicate, HAMS-1B (H-B-MFI), including the acid types, strengths, location, and quantities via multinuclear 1D/2D MAS NMR experiments using TMPO as probe molecule (Fig. 8(B)), and six types of acid sites owing to Brønsted and Lewis acid sites inside or outside of the channels were identified [129].

4 Application for multifunctional heteroatom zeolites

4.1 Biomass conversion

As a source of clean energy, biomass can be converted into liquid or gaseous high-value fuels and other chemicals. The introduction of Sn-containing BEA zeolite makes a great breakthrough in the utilization of solid Lewis acids in the aqueous-phase reactions, especially for the biomass conversion. More detailed information on the design and applications of Lewis acidic heteroatom zeolites can be found in the recent review articles [70,130]. Herein, we mainly introduce the applications of multifunctional heteroatom zeolites in cascade reaction of biomass (Table 2).

Table 2 Applications of multifunctional heteroatom zeolite for the biomass conversion

Reactant	Product	Catalyst	Conditions [a)]	$C_{reactant}$ [a)]/%	$Y_{product}$ [a)]/%	Refs.
Glucose	5-(Ethoxymethyl)furfural	MFI-Sn/Al	EtOH, 413 K, 9 h	100	44	[25]
Cortalcerone	Furylglycolic acid	Al-Sn-Beta	H_2O/MeOH, 358 K, 0.5 h	42	53 [b)]	[26]
Glucose	5-Hydroxymethylfurfural	Sn-Al-Beta	DMSO, 433 K, 4 h	60	62 [b)]	[36]
Furfural (FAL)	Bio-products	Sn-Al-Beta	2-BuOH, 393 K, 5 h	86	83 [c)]	[39]
FAL	γ-Valerolactone (GVL)	Sn-Al-Beta	2-BuOH,453 K, 24 h	100	60 [b)]	[40]
FAL	Furanic ethers	Sn-Al-Beta	2-BuOH, 393 K, 107 h on stream	100	75 [b)]	[41]
Glucose	Methyl levulinate	Sn-Al-Beta	MeOH, 453 K, 5 h	100	49	[42]
Glucose	Methyl lactate	Mg-Sn-Beta	MeOH, 443 K, 5 h	100	50	[38]
		Sn–Al-USY	MeOH, 443 K, 6 h	100	40	[43]
Levoglucosan	Lactic acid	Sn-Beta–Ca	H_2O, 463 K, 2 h, 2 MPa N_2	100	66	[44]
Glucose	Lactic acid	In–Sn-Beta	H_2O, 463 K, 2 h	100	53	[45]
		Zn–Sn-Beta	H_2O, 463 K, 2 h	> 99	54	[46]
Dihydroxyacetone	Methyl lactate	Sn-Al-MFI	MeOH, 363 K, 4 h	100	~95 [b)]	[127]
FAL	Bio-products	Zr-Al-TUD-1	2-BuOH, 393 K, 7 h	70	61[c)]	[27]
		Zr-Al-Beta	2-BuOH, 393 K, 7 h	85	76 [c)]	[27]
Cinnamaldehyde	1-Cinnamyl-2-propyl ether	Zr-Al-Beta	*i*-PrOH, 355 K, 5 h	97	94	[37]
Gurfural	Bio-products	MP-ZrAl-Beta-m	2-BuOH, 423 K, 7 h	96	93 [c)]	[48]
		ZrAl-Beta/TUD-1	2-BuOH, 423 K, 5 h	99	95 [c)]	[48]
Xylose	GVL	Zr-Al-Beta	*i*-PrOH, 463 K, 48 h	100 mol	35 mol	[47]
		Zr-Al-SCM-1	*i*-PrOH, 443 K, 28 h	100	47	[131]
		Zr-Al-Beta	*i*-PrOH, 463 K, 10 h	100	34	[132]
FAL	GVL	Meso-Zr-Al-Beta	*i*-PrOH, 393 K, 24 h	100	95	[133]
Triose	Ethyl lactate	Meso-Zr-Al-Beta	EtOH, 363 K, 0.5 h	95	86	[133]
Glucose	5-Hydroemthylfurfural	Meso-Zr-Al-Beta	DMSO, 433 K, 4 h	100	49	[133]

a) Based on the highest yield reported in the literature; b) product selectivity; c) bio-products total yield.

Several key reaction steps are usually involved in the biomass conversion, and catalysts with multiple functionalities are generally required (Fig. 9) [131]. For example, multifunctional heteroatom zeolites with Brønsted and Lewis acid sites are necessary in the tandem catalytic processes for sustainable chemical production. Typically, the Sn-Al-zeolites containing both Brønsted and Lewis acid sites are widely utilized in the tandem catalytic processes [26,35,36,39–42,127,134], including Baeyer-Villiger oxidation, 1,3-dihydroxyacetone conversion into ethyl lactate, glucose conversion into furylglycolic acid and so on. The FAL to GVL reaction can be realized over bifunctional Sn-Al-BEA zeolite, and the product selectivity can be well controlled according to balance between Brønsted and Lewis acid sites [40]. After optimization, the GVL yield over bifunctional Sn-Al-BEA zeolite (Si/Sn = 63, Si/Al = 473) could reach up to 60%.

Iglesias et al. prepared bifunctional Sn-Al-FAU zeolite via the post-synthesis approach and applied it in the glucose to methyl lactate conversion [43]. After ion exchange with alkali and alkali metal, the ratio of Brønsted to Lewis acid sites could be well controlled, which showed an important impact on the product selectivity (Fig. 10). Under identical reaction conditions, Sn-Al-FAU exhibited good catalytic performance of more than 40% methyl lactate yield and remarkable stability in the glucose to methyl lactate conversion. The synergetic effect of Brønsted and Lewis acid sites in the alkali-exchanged Ca-Sn-BEA zeolite could greatly promote the catalytic activity in the glucose to methyl lactate conversion [44]. Besides, the addition of metal Zn and In in Sn-BEA zeolite could effectively inhibit the side reaction of fructose dehydration to 5-hydroxymethylfurfural and the subsequent decomposition, thereby promoting the formation of lactic acid from glucose [45,46].

The formation of mesopores and hierarchically porous can facilitate the diffusion of large molecules within the pore channels and increase the accessibility of active sites to the substrates [135–137]. Therefore, Sn-containing zeolite with hierarchical pore structures can be utilized in the transformation of macromolecule biomass [25,42,138]. The bifunctional meso-/microporosity Sn-Al-MFI zeolite could effectively catalyze the three-step reaction of glucose to 5-(ethoxymethyl)furfural in ethanol solvent, and a high 5-(ethoxymethyl)furfural yield of 44% could be achieved. During the reaction, glucose was isomerized to fructose at the Lewis acid sites, then fructose could be dehydrated to 5-hydroxymethylfurfural, and thereafter etherified to 5-(ethoxymethyl)furfural at the Brønsted acid sites (Fig. 11).

The multifunctional Zr-Al-BEA zeolite has been also utilized as a promising catalyst in other biomass cascade reactions [27,37,47,48,132]. Li et al. constructed a multifunctional meso-Zr-Al-BEA zeolite via the post-synthesis approach, and which could be utilized as a robust catalyst for cascade reactions in biomass valorization [133]. Upon optimization, a 95% yield of GVL could be achieved. The layered mesoporous Zr-Al-SCM-1 zeolite with a large specific surface area was also prepared by a post-synthesis method to catalyze the direct conversion of xylose to GVL (Fig. 12(A)) [131]. A GVL yield of 36.4% could be achieved at 170 °C with a time-on-stream of 48 h (Fig. 12(B)). In addition, few amounts of 2-propoxy glycol

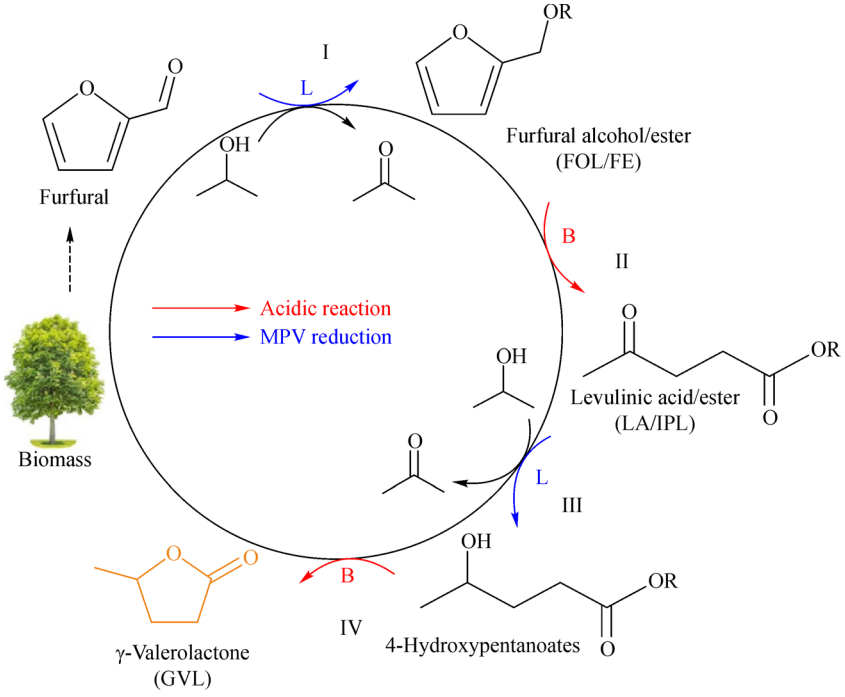

Fig. 9 Converting biomass into high value chemicals. Reprinted with permission from ref. [131], copyright 2020, Elsevier Inc.

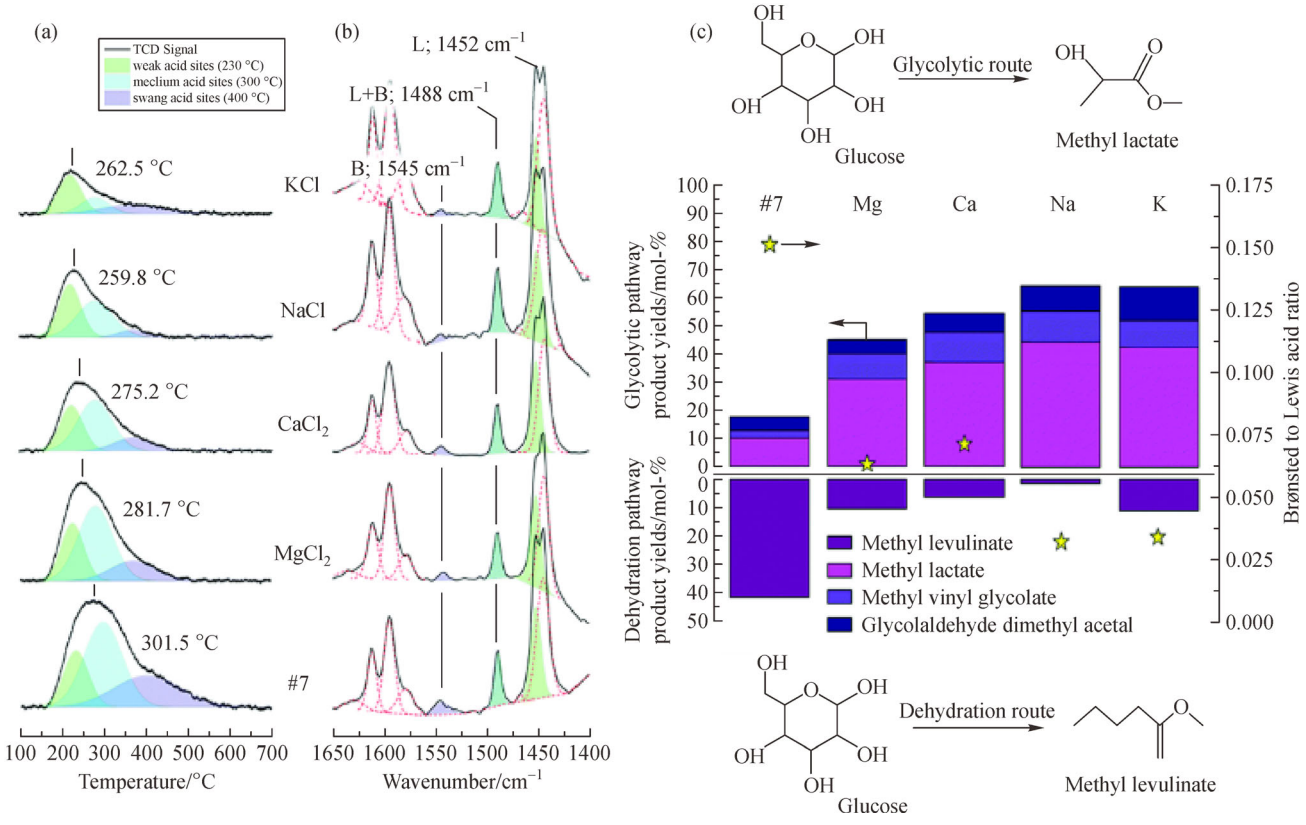

Fig. 10 (a) NH_3-TPD profiles and (b) adsorbed pyridine DRIFT spectra obtained for sample #7 mixed with aqueous solutions of alkali and alkaline-earth metal chlorides; (c) cumulative yield through different reaction pathways and Brønsted to Lewis acid ratios recorded for sample #7 and its ion-exchanged counterparts. Reprinted with permission from ref. [43], copyright 2019, Royal Society of Chemistry.

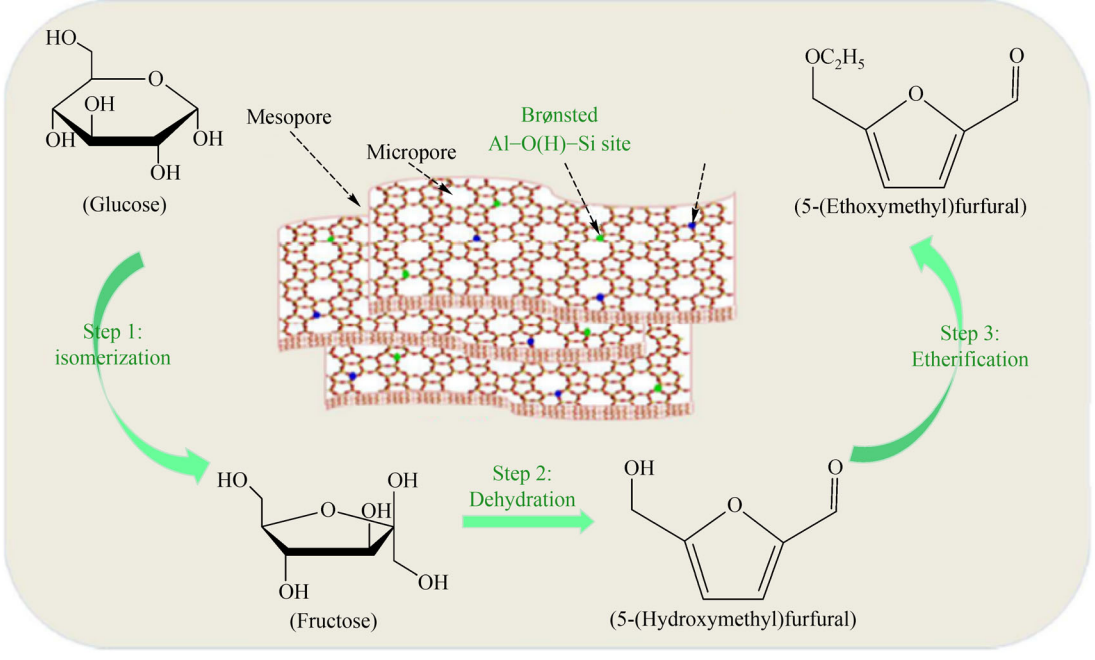

Fig. 11 Synthesis of 5-(ethoxymethyl)furfural from glucose by hierarchical multi-functional MFI-Sn/Al catalyst. Reprinted with permission from ref. [25], copyright 2018, Royal Society of Chemistry.

and 2-propyl lactate could be detected, indicating that the reaction route B was involved in this process (Fig. 12(C)). The good recyclability of multifunctional Zr-Al-SCM-1 zeolite demonstrated its great potential for applications in the tandem conversion of other biomass macromolecules.

4.2 Environmental applications

4.2.1 N_2O decomposition

Heteroatom zeolites can be used in N_2O catalytic decomposition reactions. Xu et al. prepared the bimetallic Ir/Fe-FAU zeolite by liquid-solid isomorphous substitution method, and a homogeneous dispersibility of Ir and Fe species in the zeolite framework could be achieved [57]. In addition, the formation of Al-O-Fe species and the synergistic effect between Ir and Fe sites guaranteed its excellent catalytic performance and good stability in the decomposition of N_2O.

4.2.2 Separation and detection of gases

Traditionally, zeolites are widely utilized in the gas adsorption and separation. With the development of heteroatoms zeolites, the characteristics of zeolite can be changed and might be more suitable for the specific gas adsorption and separation. Recently, Grand et al. [29] prepared highly hydrophobic W-MFI zeolite membrane to detect low-concentration exhaust gas (NO, CO, NO_2, and CO_2). The introduction of W species into the zeolite

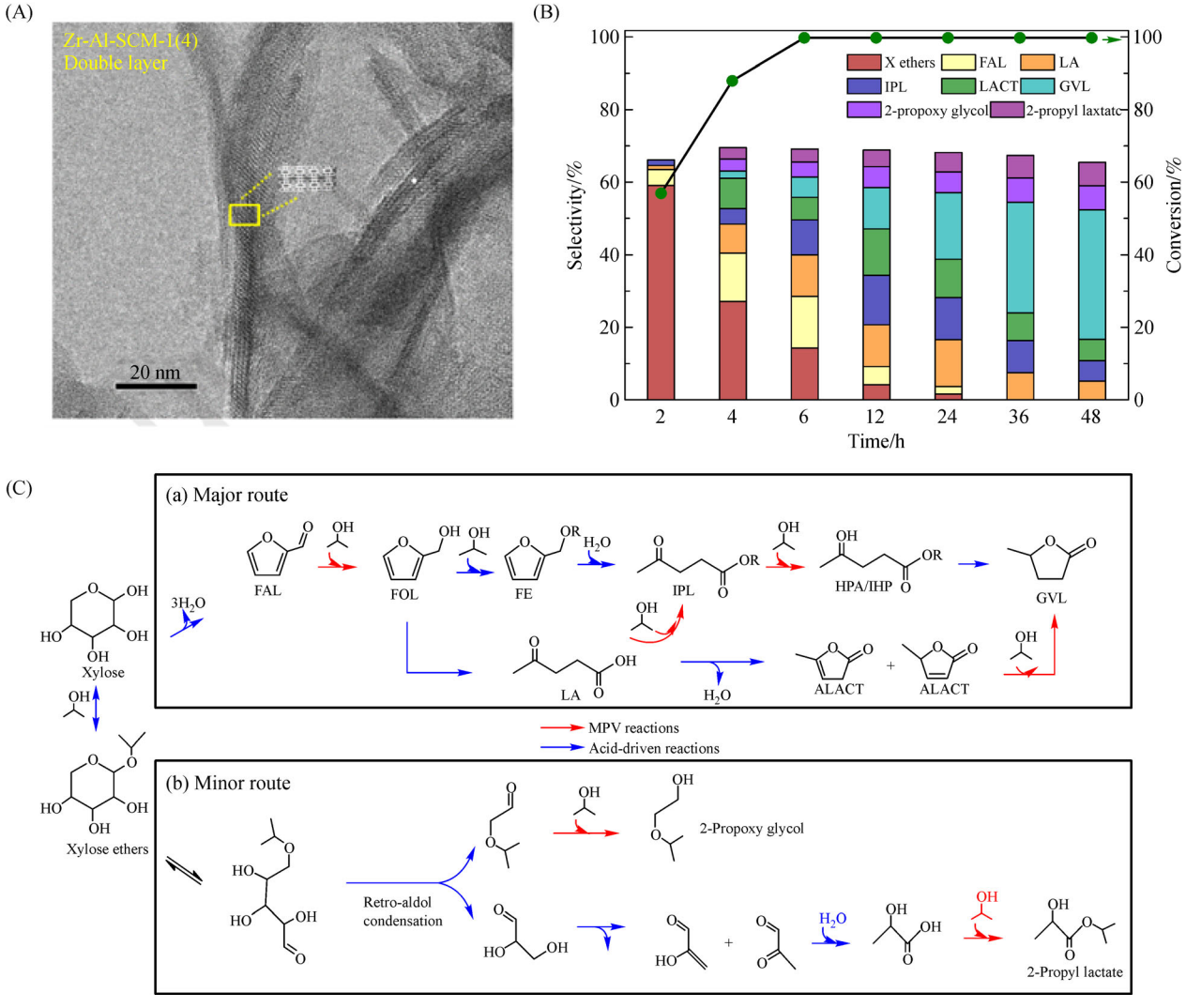

Fig. 12 (A) TEM images of Zr-Al-SCM-1; (B) xylose conversion and selectivity to products in 2-propamol over Zr-Al-SCM-1 zeolite (reaction conditions: 0.2 g xylose, 0.1 g catalyst, 10 mL isopropanol, 170 °C); (C) reaction pathway for (a) conversion of xylose and furfural into GVL through acid catalyzed (red) and MPV (blue) reactions, and (b) retro-aldol condensation of xylose into 2-propoxy glycol and 2-propyl lactate (X ethers, xylose ethers; IPL, isopropyl levulinate; LACT, α/β-angelica lactones). Reprinted with permission from ref. [131], copyright 2020, Elsevier Inc.

framework could efficiently reduce the number of hydrophilic silanol groups, thus improving the hydrophobicity of zeolite. In comparison with the traditional Si-MFI film, the heteroatom W-MFI film exhibited the higher sensitivity to low-concentration exhaust gas, even able to detect the ultra-low concentration CO_2 (1–3 ppm) and NO_2 (1 ppm) in the atmosphere. Besides, the Sn-MFI zeolite films prepared in the similar method exhibited good adsorption capacity of NO_2 and could be utilized in the selective detection of automobile exhaust [30].

4.3 Chemical synthesis

4.3.1 Ethanol conversion

Bioethanol obtained from the fermentation of sugars and starch is regarded as a most attractive renewable material to produce basic chemicals like acetaldehyde, acetic acid, isobutene, and butadiene [139,140]. In particular, the conversion of ethanol to butadiene (ETB) is becoming an attractive route since butadiene is an important monomer for the production of polymers and polymer intermediates [50,120,141]. Several key reaction steps are now generally accepted in the ETB conversion, including 1) the dehydrogenation of ethanol to acetaldehyde; 2) the aldol condensation of acetaldehyde to acetaldol; 3) the dehydration of acetaldol to crotonaldehyde; 4) the MPV reduction of crotonaldehyde to crotonyl alcohol; 5) the dehydration of crotonyl alcohol to butadiene (Fig. 13). Obviously, this is a very complicated reaction process and catalysts with multiple functionalities are required.

On the basis of the aforementioned reaction route, two independent catalytic cycles of a one-step process were proposed by Sushkevich and Ivanova, i.e., dehydrogenation of ethanol into acetaldehyde over metal sites and acetaldehyde/ethanol transformation into butadiene at Lewis acid sites [50,119]. They prepared Zr-BEA zeolite by hydrothermal synthesis first, and then loaded with Ag species by wet impregnation. Over this bifunctional Ag/Zr-BEA catalyst, a butadiene yield of 27% can be achieved. At Ag sites, the ethanol dehydrogenation to acetaldehyde occurred, while the further aldol condensation of acetaldehyde could take place on the Lewis acidic Zr sites. After combining the two species in one catalyst Ag/Zr-BEA, a synergistic effect could be well embodied and a high selectivity to butadiene was achieved. Later, an improved method for preparing bifunctional Ag/Zr-BEA zeolites was proposed, and more Zr open sites Zr(OSi)OH could be obtained. In comparison with the former Ag/Zr-BEA catalyst, the new bifunctional material with more Zr open sites exhibited strong Lewis acidity, which is beneficial to ethanol to butadiene conversion with a high butadiene productivity of 0.58 $g^{-1}\cdot h^{-1}$ and butadiene selectivity of 60%. In addition, Kyriienko et al. prepare a Ta-BEA catalyst and then doped with different metals (Zn, Ag, and Cu) for ethanol to butadiene conversion [49]. Upon optimization, high catalytic activity with 88% ethanol conversion and 73% butadiene selectivity could be achieved. Recently, Wang et al. reported a multifunctional ZnHf-MFI zeolite nanosheets for ethanol to butadiene conversion [51]. In comparison with the normal ZnHf-MFI, the nanosheet structure of the new material facilitated a higher catalytic activity in the ethanol to butadiene conversion, and a 64.6% ethanol conversion with 73% butadiene selectivity could be achieved.

4.3.2 Propane dehydrogenation

Light olefins are very important platform molecules in the petrochemical industry. Direct dehydrogenation of light alkanes offers an alternative route for olefin production in comparison with the traditional catalytic cracking or the newly established methanol-to-olefins conversion. Pt-based catalyst has been widely utilized as an effective catalyst in propane dehydrogenation to propene reaction. Wang prepared a bifunctional PtSn-BEA zeolite via a two-step post synthesis method for propane dehydrogenation reaction [52]. The framework Sn species could change the interface characteristics between Pt and zeolite support, thus promoting a high dispersion of Pt species in zeolite. Good stability and a high propene productivity of 2.3 $mol\cdot g^{-1}_{Pt}\cdot h^{-1}$ with high selectivity of >99% could be

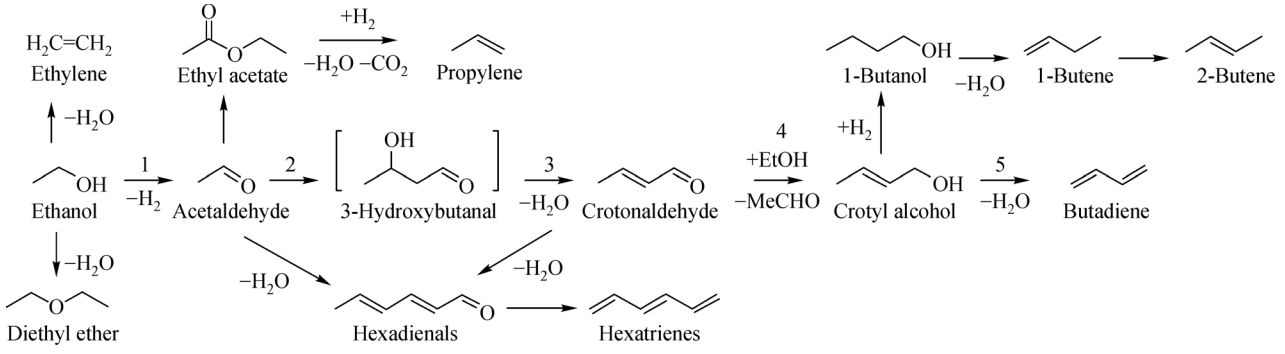

Fig. 13 Proposed reaction pathways of ethanol conversion into butadiene. Reprinted with permission from ref. [50], copyright 2016, Elsevier Inc.

achieved over PtSn-BEA zeolite catalyst. Xu et al. also prepared a Pt/Sn-BEA zeolite via the similar method for propane dehydrogenation to propylene reaction, and an initial propane conversion of 50% with a high propene selectivity of >99% could be obtained [53]. Additionally, the bifunctional TS-1 based zeolites also exhibited remarkable activity in the reaction of propane dehydrogenation. Recently, Li et al. prepared a bimetallic PtSn/TS-1 zeolite through a post-synthesis method and applied for propane dehydrogenation reaction [54]. The introduction of Sn species could effectively decrease the acidity, thus inhibiting the formation of carbon deposits on Pt surface, and consequently, a 52.4% propane conversion could be obtained.

4.3.3 Olefin epoxidation

Ti-containing zeolites such as TS-1, Ti-Beta, Ti-MWW, Ti-YNU-1, etc. have exhibited remarkable activity in selective oxidations [94,142,143]. In particular, TS-1 is most widely used in liquid phase oxidation reactions, such as epoxidation of olefins [144–147], ammoxidation of ketones [148–150], and oxidation of alcohols [151], alkanes [152] and thiophenes [153], etc. The reaction of propylene epoxidation and ammoximation of cyclohexanone has realized industrial applications. To improve the epoxide selectivity, a bifunctional palladium-modified Ti-MCM-41 molecular sieve was prepared via the post-synthesis method, followed by surface silylation with trimethylchlorosilane [55]. The Pd modification and surface silylation treatment could effectively inhibit the hydrolysis of propylene oxide, and a high propylene oxide selectivity of ~100% could be obtained.

Recently, a bifunctional TiSn-BEA zeolite was constructed by a simple and scalable post-synthesis route, and was utilized as a robust heterogeneous catalyst for the tandem conversion of alkenes to 1,2-diols [56]. The isolated Lewis acidic Ti and Sn sites within the TiSn-BEA zeolite could efficiently integrate the alkene epoxidation and the epoxide hydration in tandem in zeolite microreactor to achieve the one-step conversion of alkenes into 1,2-diols with a high selectivity of above 90% (Fig. 14).

4.3.4 Cyclohexane oxidation

Cyclohexane oxidation is an important approach to produce the chemical raw material cyclohexanone. Several heteroatom molecular sieves, such as V-MCM-41, V-MCM-48, Ce-MCM-48 and CoAlPO-5 have been utilized in the cyclohexane oxidation, but unfortunately with low catalytic activity [154–156]. In comparison with the mono-substituted heteroatom zeolites, bicomponent heteroatom zeolites can greatly enhance the catalytic activity in the cyclohexane oxidation. Liu et al. reported a bicomponent CrCoAlPO-5 zeolite for cyclohexane oxidation, and a significant enhancement of the cyclohexane conversion could be obtained due to the synergistic effect between Cr and Co active sites [31]. Zhou et al. also prepared a

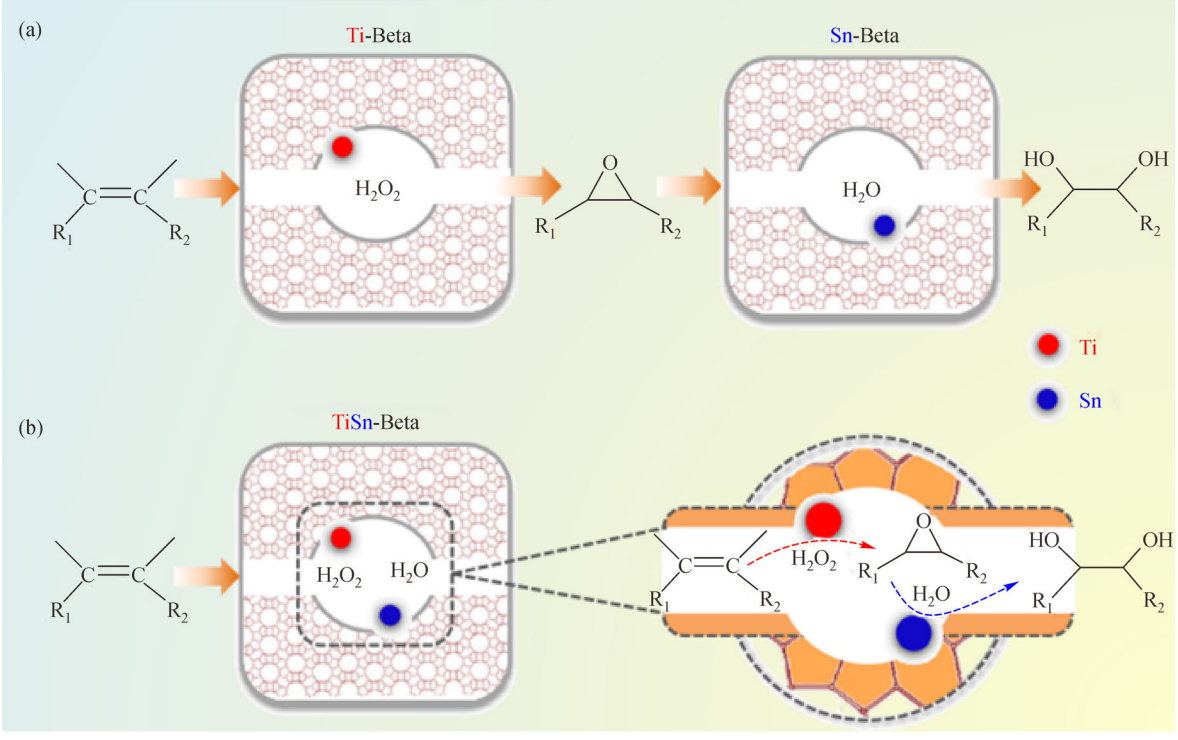

Fig. 14 Routes for the conversion of alkenes to 1,2-diols. (a) Indirect route including two processes: alkene epoxidation and epoxide hydration; (b) tandem catalytic route. Reprinted with permission from ref. [56], copyright 2021, Elsevier Inc.

multifunctional FeCoMnAlPO-5 zeolite catalyst for cyclohexane oxidation, and an obvious enhancement for the catalytic activity could be achieved [32]. With the presence of synergistic effect between multifunctional active sites, the cyclohexyl hydroperoxide intermediate can effectively decompose to cyclohexanol and cyclohexanone.

In addition, multifunctional heteroatom zeolites can be utilized in other important catalytic reactions. For example, multifunctional CuMn-BEA zeolite exhibited high activity and stability in the soot oxidation [58]. The cooperative effect between Cu^{n+} and Mn^{n+} active species in the catalyst contributed to generating highly-active oxygen species O^-/O^{2-} and NO_2 intermediate. In comparison with mono-substituted Ti-MFI and W-MFI zeolites, the bifunctional W-Ti-MFI (W-TS-1) zeolite exhibited remarkable activity in the oxidative desulfurization reaction [33]. Ga-Al-MFI with strong acid sites (formed by framework Al and Ga) as well as dehydrogenation functions (formed by the combination of Ga-oxide and zeolitic protons) exhibited good catalytic activity in low-temperature nonoxidative activation of methane [34]. SnAl-BEA zeolite with Brønsted and Lewis acid sites also exhibited good activity in the trioxanehe to polyoxymethylene dimethyl ether (OME) reaction [59]. As shown in Fig. 15, the decomposition of trioxanehe or paraformaldehyde occurred at Brønsted acid sites, while the OME formation took place at Lewis acid sites (Fig. 15).

5 Summary and outlook

As an efficient strategy to construct the catalytically active sites in zeolites and expand their catalytic applications, heteroatom zeolites have been drawn significant attentions. With heteroatom introduced into zeolite matrix, bifunctional or multifunctional zeolite-based catalysts can be obtained, which are especially suitable for complicated processes such as cascade reactions. In the past decades, significant achievements have been achieved on the construction, characterization and catalytic applications of multifunctional heteroatom zeolites. In this review article, the most representative research progresses on multifunctional heteroatom zeolites, are briefly summarized, aiming to boost further researches on this important topic. For zeolite synthesis, two main strategies, i.e., direct hydrothermal synthesis and post-synthesis modification, are introduced and compared. For zeolite characterization, several most useful techniques to identify the structural information and coordination states of heteroatoms, such as XRD, FTIR, UV-vis, Raman, XPS, XAS and ssNMR, are discussed. In the last part, the catalytic applications of multifunctional heteroatom zeolites are shown with emphasis on the synergistic effects.

Remarkable achievements have been made concerning the construction and catalytic applications of multifunctional heteroatom zeolites. However, many issues are still to be solved. According to the literature reports and our own experience, some specific challenges on multifunctional heteroatom zeolites are summarized as follows. 1) General synthesis strategies to multifunctional heteroatom zeolites. Since current synthesis strategies are more or less limited by both the types of heteroatoms and zeolites hosts, general strategies to construct the multifunctional heteroatom zeolites are being explored. Especially, a simple and scalable synthesis strategy with good reproducibility is mostly desired for industrial production. 2) Exact location of heteroatoms in zeolites and the synergistic mechanism for catalytic reactions. While the electronic and

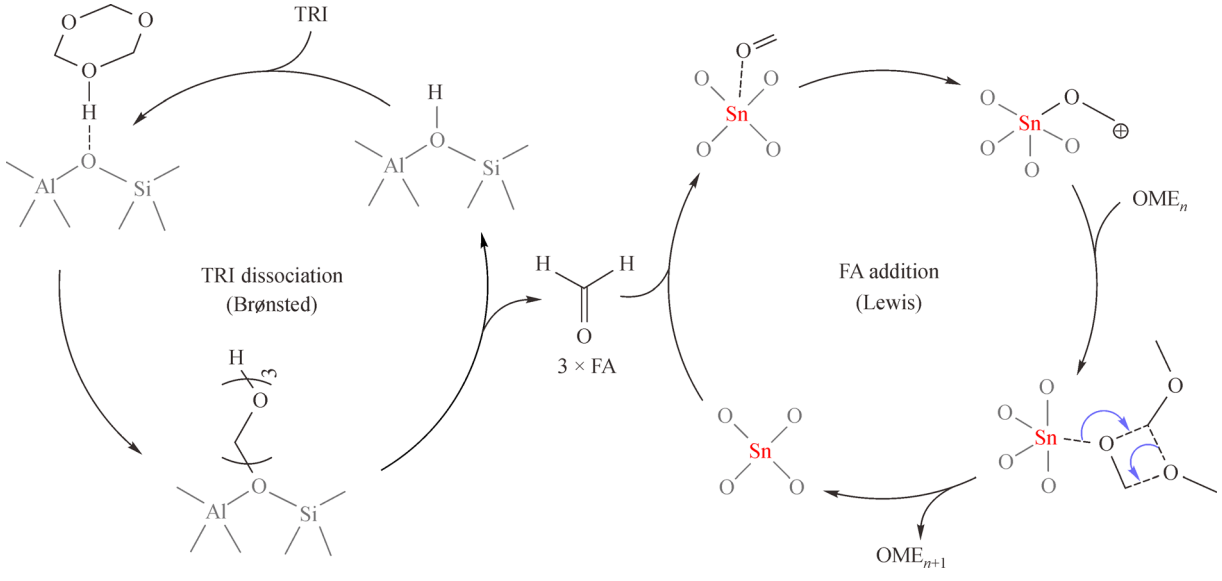

Fig. 15 Suggested reaction mechanism for the synthesis of OME from dimethoxymethane and trioxanehe with Brønsted and Lewis sites. Reprinted with permission from ref. [59], copyright 2019, Wiley-VHC.

coordination states of monocomponent in zeolite framework can be clearly identified by the combination of various techniques, it is still a challenge to identify the exact location and spatial proximity among the different heteroatoms. To solve these issues, advanced characterization technique should be developed, for example, high magnetic field ssNMR spectroscopy with the advanced methodologies might be helpful. 3) More catalytic applications of multifunctional heteroatom zeolites. Up to now, the multifunctional heteroatom zeolites have been widely utilized in a series of catalytic reactions, including biomass conversion, N_2O decomposition, propane dehydrogenation, alkene epoxidation, and so on. Nevertheless, more irreplaceable catalytic applications are expected for this unique type of materials, for example, CO_2 conversion to highly-valuable chemicals. In addition, the establishment of structure-activity relationship is of great significance for the design and optimization of multifunctional heteroatom zeolite catalysts in future studies.

Acknowledgements This work was supported by Municipal Natural Science Foundation of Tianjin (Grant No. 18JCJQJC47400), the National Natural Science Foundation of China (Grant No. 21773127) and the Fundamental Research Funds for the Central Universities.

References

1. Taramasso M, Perego G, Notari B. Preparation of porous crystalline synthetic material comprised of silicon and titanium oxides. US Patent, 4410501, 1983–10–18
2. Wroblewska A, Wajzberg J, Fajdek A, Milchert E. Epoxidation of 1-butene-3-ol over titanium silicalite TS-2 catalyst under autogenic pressure. Journal of Hazardous Materials, 2009, 163(2–3): 1303–1309
3. Gounder R, Davis M E. Titanium-Beta zeolites catalyze the stereospecific isomerization of D-glucose to L-sorbose via intramolecular C5–C1 hydride shift. ACS Catalysis, 2013, 3(7): 1469–1476
4. Song H, Wang J, Wang Z, Song H, Li F, Jin Z. Effect of titanium content on dibenzothiophene HDS performance over Ni_2P/Ti-MCM-41 catalyst. Journal of Catalysis, 2014, 311: 257–265
5. Igarashi N, Hashimoto K, Tatsumi T. Catalytical studies on trimethylsilylated Ti-MCM-41 and Ti-MCM-48 materials. Microporous and Mesoporous Materials, 2007, 104(1–3): 269–280
6. Song S, Zhao W, Wang L, Chu J, Qu J, Li S, Wang L, Qi T. One-step synthesis of Ti-MSU and its catalytic performance on phenol hydroxylation. Journal of Colloid and Interface Science, 2011, 354(2): 686–690
7. Deimund M A, Harrison L, Lunn J D, Liu Y, Malek A, Shayib R, Davis M E. Effect of heteroatom concentration in SSZ-13 on the methanol-to-olefins reaction. ACS Catalysis, 2015, 6(2): 542–550
8. Jones A J, Carr R T, Zones S I, Iglesia E. Acid strength and solvation in catalysis by MFI zeolites and effects of the identity, concentration and location of framework heteroatoms. Journal of Catalysis, 2014, 312: 58–68
9. Petkov P S, Aleksandrov H A, Valtchev V, Vayssilov G N. Framework stability of heteroatom-substituted forms of extra-large-pore Ge-silicate molecular sieves: the case of ITQ-44. Chemistry of Materials, 2012, 24(13): 2509–2518
10. Su X, Wang G, Bai X, Wu W, Xiao L, Fang Y, Zhang J. Synthesis of nanosized HZSM-5 zeolites isomorphously substituted by gallium and their catalytic performance in the aromatization. Chemical Engineering Journal, 2016, 293: 365–375
11. Luo H Y, Bui L, Gunther W R, Min E, Román-Leshkov Y. Synthesis and catalytic activity of Sn-MFI nanosheets for the Baeyer-Villiger oxidation of cyclic ketones. ACS Catalysis, 2012, 2(12): 2695–2699
12. Sun Z, Yan Y, Li G, Zhang Y, Tang Y. Microwave influence on different M–O bonds during MFI-type heteroatom (M) zeolite preparation. Industrial & Engineering Chemistry Research, 2017, 56(39): 11167–11174
13. Li X, Li B, Mao H, Shah A T. Synthesis of mesoporous zeolite Ni-MFI with high nickel contents by using the ionic complex $[(C_4H_9)_4N]_2^+[Ni(EDTA)]^{2-}$ as a template. Journal of Colloid and Interface Science, 2009, 332(2): 444–450
14. Meng L, Zhu X, Mezari B, Pestman R, Wannapakdee W, Hensen E J M. On the role of acidity in bulk and nanosheet [T]MFI (T = Al^{3+}, Ga^{3+}, Fe^{3+}, B^{3+}) zeolites in the methanol-to-hydrocarbons reaction. ChemCatChem, 2017, 9(20): 3942–3954
15. Bregante D T, Tan J Z, Sutrisno A, Flaherty D W. Heteroatom substituted zeolite FAU with ultralow Al contents for liquid-phase oxidation catalysis. Catalysis Science & Technology, 2020, 10(3): 635–647
16. Yan T, Yang L, Dai W, Wu G, Guan N, Hunger M, Li L. Cascade conversion of acetic acid to isobutene over yttrium-modified siliceous Beta zeolites. ACS Catalysis, 2019, 9(11): 9726–9738
17. Wu Y, Wang J, Liu P, Zhang W, Gu J, Wang X. Framework-substituted lanthanide MCM-22 zeolite: synthesis and characterization. Journal of the American Chemical Society, 2010, 132(51): 17989–17991
18. Reddy J K, Mantri K, Lad S, Das J, Raman G, Jasra R. Synthesis of Ce-MCM-22 and its enhanced catalytic performance for the removal of olefins from aromatic stream. Journal of Porous Materials, 2020, 27(6): 1649–1658
19. Fickel D W, D'Addio E, Lauterbach J A, Lobo R F. The ammonia selective catalytic reduction activity of copper-exchanged small-pore zeolites. Applied Catalysis B: Environmental, 2011, 102(3–4): 441–448
20. Jae J, Tompsett G A, Foster A J, Hammond K D, Auerbach S M, Lobo R F, Huber G W. Investigation into the shape selectivity of zeolite catalysts for biomass conversion. Journal of Catalysis, 2011, 279(2): 257–268
21. Luo P, Guan Y, Xu H, He M, Wu P. Postsynthesis of hierarchical core/shell ZSM-5 as an efficient catalyst in ketalation and acetalization reactions. Frontiers of Chemical Science and Engineering, 2020, 14(2): 258–266
22. Reiprich B, Weissenberger T, Schwieger W, Inayat A. Layer-like FAU-type zeolites: a comparative view on different preparation routes. Frontiers of Chemical Science and Engineering, 2020, 14(2): 127–142

23. Pang T, Yang X, Yuan C, Elzatahry A A, Alghamdi A, He X, Cheng X, Deng Y. Recent advance in synthesis and application of heteroatom zeolites. Chinese Chemical Letters, 2021, 32(1): 328–338
24. Meng B, Ren S, Li Z, Duan H, Gao X, Zhang H, Song W, Guo Q, Shen B. Intra-crystalline mesoporous zeolite [Al,Zr]-Y for catalytic cracking. ACS Applied Nano Materials, 2020, 3(9): 9293–9302
25. Bai Y, Wei L, Yang M, Chen H, Holdren S, Zhu G, Tran D T, Yao C, Sun R, Pan Y, Liu D. Three-step cascade over a single catalyst: synthesis of 5-(ethoxymethyl)furfural from glucose over a hierarchical lamellar multi-functional zeolite catalyst. Journal of Materials Chemistry. A, Materials for Energy and Sustainability, 2018, 6(17): 7693–7705
26. Schwartz T J, Goodman S M, Osmundsen C M, Taarning E, Mozuch M D, Gaskell J, Cullen D, Kersten P J, Dumesic J A. Integration of chemical and biological catalysis: production of furylglycolic acid from glucose via cortalcerone. ACS Catalysis, 2013, 3(12): 2689–2693
27. Antunes M M, Lima S, Neves P, Magalhães A L, Fazio E, Neri F, Pereira M T, Silva A F, Silva C M, Rocha S M, et al. Integrated reduction and acid-catalysed conversion of furfural in alcohol medium using Zr, Al-containing ordered micro/mesoporous silicates. Applied Catalysis B: Environmental, 2016, 182: 485–503
28. Jin Y, Asaoka S, Zhang S, Li P, Zhao S. Reexamination on transition-metal substituted MFI zeolites for catalytic conversion of methanol into light olefins. Fuel Processing Technology, 2013, 115: 34–41
29. Grand J, Talapaneni S N, Vicente A, Fernandez C, Dib E, Aleksandrov H A, Vayssilov G N, Retoux R, Boullay P, Gilson J P, et al. One-pot synthesis of silanol-free nanosized MFI zeolite. Nature Materials, 2017, 16(10): 1010–1015
30. Talapaneni S N, Grand J, Thomas S, Ahmad H A, Mintova S. Nanosized Sn-MFI zeolite for selective detection of exhaust gases. Materials & Design, 2016, 99: 574–580
31. Liu D, Zhang B, Liu X, Li J. Cyclohexane oxidation over AFI molecular sieves: effects of Cr, Co incorporation and crystal size. Catalysis Science & Technology, 2015, 5(6): 3394–3402
32. Zhou L, Xu J, Miao H, Li X, Wang F. Synthesis of FeCoMnAPO-5 molecular sieve and catalytic activity in cyclohexane oxidation by oxygen. Catalysis Letters, 2005, 99(3–4): 231–234
33. Lv G, Deng S, Yi Z, Zhang X, Wang F, Li H, Zhu Y. One-pot synthesis of framework W-doped TS-1 zeolite with robust Lewis acidity for effective oxidative desulfurization. Chemical Communications, 2019, 55(33): 4885–4888
34. Choudhary V R, Kinage A K, Choudhary T V. Low-temperature nonoxidative activation of methane over H-galloaluminosilicate (MFI) zeolite. Science, 1997, 275(5304): 1286–1288
35. Dijkmans J, Dusselier M, Gabriëls D, Houthoofd K, Magusin P C M M, Huang S, Pontikes Y, Trekels M, Vantomme A, Giebeler L, et al. Cooperative catalysis for multistep biomass conversion with Sn/Al Beta zeolite. ACS Catalysis, 2015, 5(2): 928–940
36. Li L, Ding J, Jiang J G, Zhu Z, Wu P. One-pot synthesis of 5-hydroxymethylfurfural from glucose using bifunctional [Sn,Al]-Beta catalysts. Chinese Journal of Catalysis, 2015, 36(6): 820–828
37. Li G, Gao L, Sheng Z, Zhan Y, Zhang C, Ju J, Zhang Y, Tang Y. A Zr-Al-Beta zeolite with open Zr(IV) sites: an efficient bifunctional Lewis-Brønsted acid catalyst for a cascade reaction. Catalysis Science & Technology, 2019, 9(15): 4055–4065
38. Yang X, Lv B, Lu T, Su Y, Zhou L. Promotion effect of Mg on a post-synthesized Sn-Beta zeolite for the conversion of glucose to methyl lactate. Catalysis Science & Technology, 2020, 10(3): 700–709
39. Antunes M M, Lima S, Neves P, Magalhães A L, Fazio E, Fernandes A, Neri F, Silva C M, Rocha S M, Ribeiro M F, et al. One-pot conversion of furfural to useful bio-products in the presence of a Sn, Al-containing zeolite beta catalyst prepared via post-synthesis routes. Journal of Catalysis, 2015, 329: 522–537
40. Winoto H P, Ahn B S, Jae J. Production of γ-valerolactone from furfural by a single-step process using Sn-Al-Beta zeolites: optimizing the catalyst acid properties and process conditions. Journal of Industrial and Engineering Chemistry, 2016, 40: 62–71
41. Padovan D, Al-Nayili A, Hammond C. Bifunctional Lewis and Brønsted acidic zeolites permit the continuous production of bio-renewable furanic ethers. Green Chemistry, 2017, 19(12): 2846–2854
42. Yang X, Yang J, Gao B, Lu T, Zhou L. Conversion of glucose to methyl levulinate over Sn-Al-β zeolite: role of Sn and mesoporosity. Catalysis Communications, 2019, 130: 105783
43. Iglesias J, Moreno J, Morales G, Melero J A, Juárez P, López-Granados M, Mariscal R, Martínez-Salazar I. Sn-Al-USY for the valorization of glucose to methyl lactate: switching from hydrolytic to retro-aldol activity by alkaline ion exchange. Green Chemistry, 2019, 21(21): 5876–5885
44. Hu W, Chi Z, Wan Y, Wang S, Lin J, Wan S, Wang Y. Synergetic effect of Lewis acid and base in modified Sn-β on the direct conversion of levoglucosan to lactic acid. Catalysis Science & Technology, 2020, 10(9): 2986–2993
45. Xia M, Dong W, Shen Z, Xiao S, Chen W, Gu M, Zhang Y. Efficient production of lactic acid from biomass-derived carbohydrates under synergistic effects of indium and tin in In-Sn-Beta zeolites. Sustainable Energy & Fuels, 2020, 4(10): 5327–5338
46. Dong W, Shen Z, Peng B, Gu M, Zhou X, Xiang B, Zhang Y. Selective chemical conversion of sugars in aqueous solutions without alkali to lactic acid over a Zn-Sn-Beta lewis acid-base catalyst. Scientific Reports, 2016, 6(1): 26713
47. Hernández B, Iglesias J, Morales G, Paniagua M, López-Aguado C, García Fierro J L, Wolf P, Hermans I, Melero J A. One-pot cascade transformation of xylose into γ-valerolactone (GVL) over bifunctional Brønsted-Lewis Zr-Al-beta zeolite. Green Chemistry, 2016, 18(21): 5777–5781
48. Antunes M M, Neves P, Fernandes A, Lima S, Silva A F, Ribeiro M F, Silva C M, Pillinger M, Valente A A. Bulk and composite catalysts combining BEA topology and mesoporosity for the valorisation of furfural. Catalysis Science & Technology, 2016, 6(21): 7812–7829
49. Kyriienko P I, Larina O V, Soloviev S O, Orlyk S M, Calers C, Dzwigaj S. Ethanol conversion into 1,3-butadiene by the lebedev method over MTaSiBEA zeolites (M = Ag, Cu, Zn). ACS Sustainable Chemistry & Engineering, 2017, 5(3): 2075–2083
50. Sushkevich V L, Ivanova I I. Ag-promoted ZrBEA zeolites obtained by post-synthetic modification for conversion of ethanol to butadiene. ChemSusChem, 2016, 9(16): 2216–2225

51. Wang C, Zheng M, Li X, Li X, Zhang T. Catalytic conversion of ethanol into butadiene over high performance LiZnHf-MFI zeolite nanosheets. Green Chemistry, 2019, 21(5): 1006–1010
52. Wang Y, Hu Z P, Tian W, Gao L, Wang Z, Yuan Z Y. Framework-confined Sn in Si-beta stabilizing ultra-small Pt nanoclusters as direct propane dehydrogenation catalysts with high selectivity and stability. Catalysis Science & Technology, 2019, 9(24): 6993–7002
53. Xu Z, Yue Y, Bao X, Xie Z, Zhu H. Propane dehydrogenation over Pt clusters localized at the Sn single-site in zeolite framework. ACS Catalysis, 2019, 10(1): 818–828
54. Li J, Li J, Zhao Z, Fan X, Liu J, Wei Y, Duan A, Xie Z, Liu Q. Size effect of TS-1 supports on the catalytic performance of PtSn/TS-1 catalysts for propane dehydrogenation. Journal of Catalysis, 2017, 352: 361–370
55. Liu J, Fang S, Jian R, Wu F, Jian P. Silylated Pd/Ti-MCM-41 catalyst for the selective production of propylene oxide from the oxidation of propylene with cumene hydroperoxide. Powder Technology, 2018, 329: 19–24
56. Lei Q, Wang C, Dai W, Wu G, Guan N, Hunger M, Li L. Tandem Lewis acid catalysis for the conversion of alkenes to 1,2-diols in the confined space of bifunctional TiSn-Beta zeolite. Chinese Journal of Catalysis, 2021, 42(7): 1176–1184
57. Shen Q, Li L, Hao Z, Xu Z P. Highly active and stable bimetallic Ir/Fe-USY catalysts for direct and NO-assisted N_2O decomposition. Applied Catalysis B: Environmental, 2008, 84(3–4): 734–741
58. Zhou X, Chen H, Zhang G, Wang J, Xie Z, Hua Z, Zhang L, Shi J. Cu/Mn co-loaded hierarchically porous zeolite beta: a highly efficient synergetic catalyst for soot oxidation. Journal of Materials Chemistry. A, Materials for Energy and Sustainability, 2015, 3(18): 9745–9753
59. Baranowski C J, Roger M, Bahmanpour A M, Krocher O. Nature of synergy between Brønsted and Lewis acid sites in Sn-Beta zeolites for polyoxymethylene dimethyl ethers synthesis. ChemSusChem, 2019, 12(19): 4421–4431
60. Chae H J, Park S S, Shin Y H, Park M B. Synthesis and characterization of nanocrystalline TiAPSO-34 catalysts and their performance in the conversion of methanol to light olefins. Microporous and Mesoporous Materials, 2018, 259: 60–66
61. Wróblewska A. Water as the solvent for the process of phenol hydroxylation over the Ti-MWW catalyst. Reaction Kinetics, Mechanisms and Catalysis, 2012, 108(2): 491–505
62. Wang B, Peng X, Yang J, Lin M, Zhu B, Zhang Y, Xia C, Liao W, Shu X. Nano-crystalline, hierarchical zeolite Ti-Beta: hydrothermal synthesis and catalytic performance in alkenes epoxidation reactions. Microporous and Mesoporous Materials, 2019, 278: 30–34
63. Li J, Corma A, Yu J. Synthesis of new zeolite structures. Chemical Society Reviews, 2015, 44(20): 7112–7127
64. Moliner M, Rey F, Corma A. Towards the rational design of efficient organic structure-directing agents for zeolite synthesis. Angewandte Chemie International Edition, 2013, 52(52): 13880–13889
65. Moliner M, Corma A. Advances in the synthesis of titanosilicates: from the medium pore TS-1 zeolite to highly-accessible ordered materials. Microporous and Mesoporous Materials, 2014, 189: 31–40
66. Corma A, Domine M E, Nemeth L, Valencia S. Al-free Sn-Beta zeolite as a catalyst for the selective reduction of carbonyl compounds (Meerwein-Ponndorf-Verley reaction). Journal of the American Chemical Society, 2002, 124(13): 3194–3195
67. Corma A, Nemeth L T, Renz M, Valencia S. Sn-zeolite beta as a heterogeneous chemoselective catalyst for Baeyer-Villiger oxidations. Nature, 2001, 412(6845): 423–425
68. Corma A, Llabrés i Xamena F X, Prestipino C, Renz M, Valencia S. Water resistant, catalytically active Nb and Ta isolated lewis acid sites, homogeneously distributed by direct synthesis in a Beta zeolite. Journal of Physical Chemistry C, 2009, 113(26): 11306–11315
69. Corma A. Water-resistant solid lewis acid catalysts: Meerwein-Ponndorf-Verley and oppenauer reactions catalyzed by tin-beta zeolite. Journal of Catalysis, 2003, 215(2): 294–304
70. Dapsens P Y, Mondelli C, Perez-Ramirez J. Design of Lewis-acid centres in zeolitic matrices for the conversion of renewables. Chemical Society Reviews, 2015, 44(20): 7025–7043
71. Niphadkar P S, Kotwal M S, Deshpande S S, Bokade V V, Joshi P N. Tin-silicalite-1: synthesis by dry gel conversion, characterization and catalytic performance in phenol hydroxylation reaction. Materials Chemistry and Physics, 2009, 114(1): 344–349
72. Kang Z, Zhang X, Liu H, Qiu J, Yeung K L. A rapid synthesis route for Sn-Beta zeolites by steam-assisted conversion and their catalytic performance in Baeyer-Villiger oxidation. Chemical Engineering Journal, 2013, 218: 425–432
73. Li P, Liu G, Wu H, Liu Y, Jiang J G, Wu P. Postsynthesis and selective oxidation properties of nanosized Sn-Beta zeolite. Journal of Physical Chemistry C, 2011, 115(9): 3663–3670
74. Jin J, Ye X, Li Y, Wang Y, Li L, Gu J, Zhao W, Shi J. Synthesis of mesoporous Beta and Sn-Beta zeolites and their catalytic performances. Dalton Transactions (Cambridge, England), 2014, 43(22): 8196–8204
75. Dzwigaj S, Nogier J P, Che M, Saito M, Hosokawa T, Thouverez E, Matsuoka M, Anpo M. Influence of the Ti content on the photocatalytic oxidation of 2-propanol and CO on TiSiBEA zeolites. Catalysis Communications, 2012, 19: 17–20
76. Dijkmans J, Gabriëls D, Dusselier M, de Clippel F, Vanelderen P, Houthoofd K, Malfliet A, Pontikes Y, Sels B F. Productive sugar isomerization with highly active Sn in dealuminated β zeolites. Green Chemistry, 2013, 15(10): 2777–2785
77. Tielens F, Shishido T, Dzwigaj S. What do tantalum framework sites look like in zeolites? A combined theoretical and experimental investigation. Journal of Physical Chemistry C, 2010, 114(21): 9923–9930
78. Nogier J P, Millot Y, Man P P, Shishido T, Che M, Dzwigaj S. Probing the incorporation of Ti(IV) into the BEA zeolite framework by XRD, FTIR, NMR, and DR UV. Journal of Physical Chemistry C, 2009, 113(12): 4885–4889
79. Dzwigaj S, Millot Y, Méthivier C, Che M. Incorporation of Nb(V) into BEA zeolite investigated by XRD, NMR, IR, DR UV-vis, and XPS. Microporous and Mesoporous Materials, 2010, 130(1–3): 162–166
80. Janas J, Gurgul J, Socha R P, Shishido T, Che M, Dzwigaj S. Selective catalytic reduction of NO by ethanol: speciation of iron and “structure-properties” relationship in FeSiBEA zeolite.

Applied Catalysis B: Environmental, 2009, 91(1–2): 113–122
81. Dzwigaj S, Che M. Toward redox framework single site zeolite catalysts. Catalysis Today, 2011, 169(1): 232–241
82. Tang B, Dai W, Sun X, Wu G, Li L, Guan N, Hunger M. Incorporation of cerium atoms into Al-free Beta zeolite framework for catalytic application. Chinese Journal of Catalysis, 2015, 36(6): 801–805
83. Tang B, Dai W, Wu G, Guan N, Li L, Hunger M. Improved postsynthesis strategy to Sn-Beta zeolites as lewis acid catalysts for the ring-opening hydration of epoxides. ACS Catalysis, 2014, 4(8): 2801–2810
84. Tang B, Dai W, Sun X, Wu G, Guan N, Hunger M, Li L. Mesoporous Zr-Beta zeolites prepared by a post-synthetic strategy as a robust Lewis acid catalyst for the ring-opening aminolysis of epoxides. Green Chemistry, 2015, 17(3): 1744–1755
85. Ding J, Xu L, Yu Y, Wu H, Huang S, Yang Y, Wu J, Wu P. Clean synthesis of acetaldehyde oxime through ammoximation on titanosilicate catalysts. Catalysis Science & Technology, 2013, 3(10): 2587–2595
86. Śrębowata A, Baran R, Łomot D, Lisovytskiy D, Onfroy T, Dzwigaj S. Remarkable effect of postsynthesis preparation procedures on catalytic properties of Ni-loaded BEA zeolites in hydrodechlorination of 1,2-dichloroethane. Applied Catalysis B: Environmental, 2014, 147: 208–220
87. Ren W, Hua Z, Ge T, Zhou X, Chen L, Zhu Y, Shi J. Post-synthesis of hierarchically structured Ti-β zeolites and their epoxidation catalytic performance. Chinese Journal of Catalysis, 2015, 36(6): 906–912
88. Dai W, Lei Q, Wu G, Guan N, Hunger M, Li L. Spectroscopic signature of lewis acidic framework and extraframework Sn sites in Beta zeolites. ACS Catalysis, 2020, 10(23): 14135–14146
89. Niphadkar P S, Bhange D S, Selvaraj K, Joshi P N. Thermal expansion properties of stannosilicate molecular sieve with MFI type structure. Chemical Physics Letters, 2012, 548: 51–54
90. Kore R, Srivastava R, Satpati B. Highly efficient nanocrystalline zirconosilicate catalysts for the aminolysis, alcoholysis, and hydroamination reactions. ACS Catalysis, 2013, 3(12): 2891–2904
91. Guo Q, Feng Z, Li G, Fan F, Li C. Finding the "missing components" during the synthesis of TS-1 zeolite by UV resonance Raman spectroscopy. Journal of Physical Chemistry C, 2013, 117(6): 2844–2848
92. Yan M, Jin F, Ding Y, Wu G, Chen R, Wang L, Yan Y. Synthesis of titanium-incorporated MWW zeolite by sequential deboronation and atom-planting treatment of ERB-1 as an epoxidation catalyst. Industrial & Engineering Chemistry Research, 2019, 58(12): 4764–4773
93. Yue Y, Liu H, Yuan P, Yu C, Bao X. One-pot synthesis of hierarchical FeZSM-5 zeolites from natural aluminosilicates for selective catalytic reduction of NO by NH_3. Scientific Reports, 2015, 5(1): 9270
94. Tang B, Dai W, Sun X, Guan N, Li L, Hunger M. A procedure for the preparation of Ti-Beta zeolites for catalytic epoxidation with hydrogen peroxide. Green Chemistry, 2014, 16(4): 2281–2291
95. Chen Y, Wang X, Zhang L. Identifying the elusive framework niobium in NbS-1 zeolite by UV resonance raman spectroscopy. ChemPhysChem, 2017, 18(23): 3325–3328
96. Ju X, Tian F, Wang Y, Fan F, Feng Z, Li C. A novel synthetic strategy of Fe-ZSM-35 with pure framework Fe species and its formation mechanism. Inorganic Chemistry Frontiers, 2018, 5(8): 2031–2037
97. Zhou H, Zhu W, Shi L, Liu H, Liu S, Xu S, Ni Y, Liu Y, Li L, Liu Z. Promotion effect of Fe in mordenite zeolite on carbonylation of dimethyl ether to methyl acetate. Catalysis Science & Technology, 2015, 5(3): 1961–1968
98. Xiong G, Cao Y, Guo Z, Jia Q, Tian F, Liu L. The roles of different titanium species in TS-1 zeolite in propylene epoxidation studied by *in situ* UV Raman spectroscopy. Physical Chemistry Chemical Physics, 2016, 18(1): 190–196
99. Jin S, Wang Z, Tao G, Zhang S, Liu W, Fu W, Zhang B, Sun H, Wang Y, Yang W. UV resonance Raman spectroscopic insight into titanium species and structure-performance relationship in boron-free Ti-MWW zeolite. Journal of Catalysis, 2017, 353: 305–314
100. Guo Q, Sun K, Feng Z, Li G, Guo M, Fan F, Li C. A thorough investigation of the active titanium species in TS-1 zeolite by *in situ* UV resonance raman spectroscopy. Chemistry (Weinheim an der Bergstrasse, Germany), 2012, 18(43): 13854–13860
101. Fan F, Feng Z, Li C U V. Raman spectroscopic studies on active sites and synthesis mechanisms of transition metal-containing microporous and mesoporous materials. Accounts of Chemical Research, 2010, 43(3): 378–387
102. Zhang S, Jin S, Tao G, Wang Z, Liu W, Chen Y, Luo J, Zhang B, Sun H, Wang Y, Yang W. The evolution of titanium species in boron-containing Ti-MWW zeolite during post-treatment revealed by UV resonance Raman spectroscopy. Microporous and Mesoporous Materials, 2017, 253: 183–190
103. Zhao J, Zhang Y, Zhang S, Wang Q, Chen M, Hu T, Meng C. Synthesis and characterization of Mn-silicalite-1 by the hydrothermal conversion of Mn-magadiite under the neutral condition and its catalytic performance on selective oxidation of styrene. Microporous and Mesoporous Materials, 2018, 268: 16–24
104. Xia C, Liu Y, Lin M, Peng X, Zhu B, Shu X. Confirmation of the isomorphous substitution by Sn atoms in the framework positions of MFI-typed zeolite. Catalysis Today, 2018, 316: 193–198
105. Nakai M, Miyake K, Inoue R, Ono K, Al Jabri H, Hirota Y, Uchida Y, Tanaka S, Miyamoto M, Oumi Y, et al. Dehydrogenation of propane over high silica *BEA type gallosilicate (Ga-Beta). Catalysis Science & Technology, 2019, 9(22): 6234–6239
106. Simancas R, Nishitoba T, Park S, Kondo J N, Rey F, Gies H, Yokoi T. Versatile phosphorus-structure-directing agent for direct preparation of novel metallosilicate zeolites with IFW-topology. Microporous and Mesoporous Materials, 2021, 317: 111005
107. Sushkevich V L, Kots P A, Kolyagin Y G, Yakimov A V, Marikutsa A V, Ivanova I I. Origin of water-induced Brønsted acid sites in Sn-BEA zeolites. Journal of Physical Chemistry C, 2019, 123(9): 5540–5548
108. Gunther W R, Michaelis V K, Caporini M A, Griffin R G, Roman-Leshkov Y. Dynamic nuclear polarization NMR enables the analysis of Sn-Beta zeolite prepared with natural abundance ^{119}Sn precursors. Journal of the American Chemical Society, 2014, 136(17): 6219–6222
109. Wolf P, Valla M, Rossini A J, Comas-Vives A, Nunez-Zarur F, Malaman B, Lesage A, Emsley L, Coperet C, Hermans I. NMR

signatures of the active sites in Sn-beta zeolite. Angewandte Chemie International Edition, 2014, 53(38): 10179–10183
110. Qi G, Wang Q, Xu J, Wu Q, Wang C, Zhao X, Meng X, Xiao F, Deng F. Direct observation of tin sites and their reversible interconversion in zeolites by solid-state NMR spectroscopy. Communications Chemistry, 2018, 1(1): 22
111. Senamart N, Buttha S, Pantupho W, Koleva I Z, Loiha S, Aleksandrov H A, Wittayakun J, Vayssilov G N. Characterization and temperature evolution of iron-containing species in HZSM-5 zeolite prepared from different iron sources. Journal of Porous Materials, 2019, 26(4): 1227–1240
112. Nemeth L, Moscoso J, Erdman N, Bare S R, Oroskar A, Kelly S D, Corma A, Valencia S, Renz M. Synthesis and characterization of Sn-Beta as a selective oxidation catalyst. Studies in Surface Science and Catalysis, 2004, 154(4): 2626–2631
113. Gabrienko A A, Arzumanov S S, Toktarev A V, Danilova I G, Prosvirin I P, Kriventsov V V, Zaikovskii V I, Freude D, Stepanov A G. Different efficiency of Zn^{2+} and ZnO species for methane activation on Zn-modified zeolite. ACS Catalysis, 2017, 7(3): 1818–1830
114. Qin J, Li B S, Yan D P. Synthesis, characterization and catalytic performance of well-ordered crystalline heteroatom mesoporous MCM-41. Crystals, 2017, 7(4): 89–99
115. Berlier G, Pourny M, Bordiga S, Spoto G, Zecchina A, Lamberti C. Coordination and oxidation changes undergone by iron species in Fe-MCM-22 upon template removal, activation and redox treatments: an *in situ* IR, EXAFS and XANES study. Journal of Catalysis, 2005, 229(1): 45–54
116. Bordiga S, Groppo E, Agostini G, van Bokhoven J A, Lamberti C. Reactivity of surface species in heterogeneous catalysts probed by *in situ* X-ray absorption techniques. Chemical Reviews, 2013, 113(3): 1736–1850
117. Aponte Y, de Lasa H. The Effect of Zn on offretite zeolite properties. Acidic characterizations and NH_3-TPD desorption models. Industrial & Engineering Chemistry Research, 2017, 56(8): 1948–1960
118. Srinivas D, Srivastava R, Ratnasamy P. Transesterifications over titanosilicate molecular sieves. Catalysis Today, 2004, 96(3): 127–133
119. Sushkevich V L, Ivanova I I, Taarning E. Ethanol conversion into butadiene over Zr-containing molecular sieves doped with silver. Green Chemistry, 2015, 17(4): 2552–2559
120. Sushkevich V L, Vimont A, Travert A, Ivanova I I. Spectroscopic evidence for open and closed Lewis acid sites in ZrBEA zeolites. Journal of Physical Chemistry C, 2015, 119(31): 17633–17639
121. Sushkevich V L, Palagin D, Ivanova I I. With open arms: open sites of ZrBEA zeolite facilitate selective synthesis of butadiene from ethanol. ACS Catalysis, 2015, 5(8): 4833–4836
122. Zheng A, Deng F, Liu S B. Acidity characterization of solid acid catalysts by solid-state ^{31}P NMR of adsorbed phosphorus-containing probe molecules. Annual Reports on NMR Spectroscopy, 2014, 81: 47–108
123. Dubray F, Moldovan S, Kouvatas C, Grand J, Aquino C, Barrier N, Gilson J P, Nesterenko N, Minoux D, Mintova S. Direct evidence for single molybdenum atoms incorporated in the framework of MFI zeolite nanocrystals. Journal of the American Chemical Society, 2019, 141(22): 8689–8693
124. Dyballa M, Rieg C, Dittmann D, Li Z, Buchmeiser M, Plietker B, Hunger M. Potential of triphenylphosphine as solid-state NMR probe for studying the noble metal distribution on porous supports. Microporous and Mesoporous Materials, 2020, 293: 109778
125. Yi X, Ko H H, Deng F, Liu S B, Zheng A. Solid-state ^{31}P NMR mapping of active centers and relevant spatial correlations in solid acid catalysts. Nature Protocols, 2020, 15(10): 3527–3555
126. Zheng A, Liu S B, Deng F. 31P NMR Chemical shifts of phosphorus probes as reliable and practical acidity scales for solid and liquid catalysts. Chemical Reviews, 2017, 117(19): 12475–12531
127. Yuan E, Dai W, Wu G, Guan N, Hunger M, Li L. Facile synthesis of Sn-containing MFI zeolites as versatile solid acid catalysts. Microporous and Mesoporous Materials, 2018, 270: 265–273
128. Zhao R, Zhao Z, Li S, Zhang W. Insights into the correlation of aluminum distribution and Brønsted acidity in H-Beta zeolites from solid-state NMR spectroscopy and DFT calculations. Journal of Physical Chemistry Letters, 2017, 8(10): 2323–2327
129. Wiper P V, Amelse J, Mafra L. Multinuclear solid-state NMR characterization of the Brønsted/Lewis acid properties in the BP HAMS-1B (H-[B]-ZSM-5) borosilicate molecular sieve using adsorbed TMPO and TBPO probe molecules. Journal of Catalysis, 2014, 316: 240–250
130. Ennaert T, Van Aelst J, Dijkmans J, De Clercq R, Schutyser W, Dusselier M, Verboekend D, Sels B F. Potential and challenges of zeolite chemistry in the catalytic conversion of biomass. Chemical Society Reviews, 2016, 45(3): 584–611
131. Li X, Yuan X, Xia G, Liang J, Liu C, Wang Z, Yang W. Catalytic production of γ-valerolactone from xylose over delaminated Zr-Al-SCM-1 zeolite via a cascade process. Journal of Catalysis, 2020, 392: 175–185
132. Melero J A, Morales G, Iglesias J, Paniagua M, López-Aguado C, Wilson K, Osatiashtiani A. Efficient one-pot production of γ-valerolactone from xylose over Zr-Al-Beta zeolite: rational optimization of catalyst synthesis and reaction conditions. Green Chemistry, 2017, 19(21): 5114–5121
133. Song S, Di L, Wu G, Dai W, Guan N, Li L. Meso-Zr-Al-beta zeolite as a robust catalyst for cascade reactions in biomass valorization. Applied Catalysis B: Environmental, 2017, 205: 393–403
134. van der Graaff W N P, Tempelman C H L, Pidko E A, Hensen E J M. Influence of pore topology on synthesis and reactivity of Sn-modified zeolite catalysts for carbohydrate conversions. Catalysis Science & Technology, 2017, 7(14): 3151–3162
135. Diao Z, Cheng L, Guo W, Hou X, Zheng P, Zhou Q. Fabrication and catalytic performance of meso-ZSM-5 zeolite encapsulated ferric oxide nanoparticles for phenol hydroxylation. Frontiers of Chemical Science and Engineering, 2020, 15(3): 643–653
136. Hou Y, Li X, Sun M, Li C, Su B L, Lei K, Yu S, Wang Z, Hu Z, Chen L, et al. The effect of hierarchical single-crystal ZSM-5 zeolites with different Si/Al ratios on its pore structure and catalytic performance. Frontiers of Chemical Science and Engineering, 2020, 15(2): 269–278
137. Wang D, Sun H, Liu W, Shen Z, Yang W. Hierarchical ZSM-5 zeolite with radial mesopores: preparation, formation mechanism

and application for benzene alkylation. Frontiers of Chemical Science and Engineering, 2019, 14(2): 248–257

138. Zhang J, Wang L, Wang G, Chen F, Zhu J, Wang C, Bian C, Pan S, Xiao F S. Hierarchical Sn-Beta zeolite catalyst for the conversion of sugars to alkyl lactates. ACS Sustainable Chemistry & Engineering, 2017, 5(4): 3123–3131
139. Makshina E V, Dusselier M, Janssens W, Degreve J, Jacobs P A, Sels B F. Review of old chemistry and new catalytic advances in the on-purpose synthesis of butadiene. Chemical Society Reviews, 2014, 43(22): 7917–7953
140. Sun J, Wang Y. Recent advances in catalytic conversion of ethanol to chemicals. ACS Catalysis, 2014, 4(4): 1078–1090
141. Kyriienko P I, Larina O V, Soloviev S O, Orlyk S M, Dzwigaj S. High selectivity of TaSiBEA zeolite catalysts in 1,3-butadiene production from ethanol and acetaldehyde mixture. Catalysis Communications, 2016, 77: 123–126
142. Lu X, Xu H, Yan J, Zhou W J, Liebens A, Wu P. One-pot synthesis of ethylene glycol by oxidative hydration of ethylene with hydrogen peroxide over titanosilicate catalysts. Journal of Catalysis, 2018, 358: 89–99
143. Ruan J, Wu P, Slater B, Terasaki O. Structure elucidation of the highly active titanosilicate catalyst Ti-YNU-1. Angewandte Chemie International Edition, 2005, 117(41): 6877–6881
144. Jiao W, He Y, Li J, Wang J, Tatsumi T, Fan W. Ti-rich TS-1: a highly active catalyst for epoxidation of methallyl chloride to 2-methyl epichlorohydrin. Applied Catalysis A, General, 2015, 491: 78–85
145. Ok D Y, Jiang N, Prasetyanto E A, Jin H, Park S E. Epoxidation of cyclic-olefins over carbon template mesoporous TS-1. Microporous and Mesoporous Materials, 2011, 141(1–3): 2–7
146. Tekla J, Tarach K A, Olejniczak Z, Girman V, Góra-Marek K. Effective hierarchization of TS-1 and its catalytic performance in cyclohexene epoxidation. Microporous and Mesoporous Materials, 2016, 233: 16–25
147. Wang B, Lu L, Ge B, Chen S, Zhu J, Wei D. Hydrophobic and hierarchical modification of TS-1 and application for propylene epoxidation. Journal of Porous Materials, 2018, 26(1): 227–237
148. Dal Pozzo L, Fornasari G, Monti T. TS-1, catalytic mechanism in cyclohexanone oxime production. Catalysis Communications, 2002, 3(8): 369–375
149. Li Z, Chen R, Xing W, Jin W, Xu N. Continuous acetone ammoximation over TS-1 in a tubular membrane reactor. Industrial & Engineering Chemistry Research, 2010, 49(14): 6309–6316
150. Xin H, Zhao J, Xu S, Li J, Zhang W, Guo X, Hensen E J M, Yang Q, Li C. Enhanced catalytic oxidation by hierarchically structured TS-1 zeolite. Journal of Physical Chemistry C, 2010, 114(14): 6553–6559
151. Maspero F, Romano U. Oxidation of alcohols with H_2O_2 catalyzed by titanium silicalite-1. Journal of Catalysis, 1994, 146(2): 476–482
152. Schuster W, Niederer J P M, Hoelderich W F. The gas phase oxidative dehydrogenation of propane over TS-1. Applied Catalysis A, General, 2001, 209(1–2): 131–143
153. Kong L, Li G, Wang X. Mild oxidation of thiophene over TS-1/H_2O_2. Catalysis Today, 2004, 93: 341–345
154. Dapurkar S E, Sakthivel A, Selvam P. Mesoporous VMCM-41: highly efficient and remarkable catalyst for selective oxidation of cyclohexane to cyclohexanol. Journal of Molecular Catalysis A Chemical, 2004, 223(1–2): 241–250
155. Fan W, Fan B, Song M, Chen T, Li R, Dou T, Tatsumi T, Weckhuysen B M. Synthesis, characterization and catalysis of (Co, V)-, (Co, Cr)- and (Cr, V)APO-5 molecular sieves. Microporous and Mesoporous Materials, 2006, 94(1–3): 348–357
156. Selvam P, Dapurkar S E. Catalytic activity of highly ordered mesoporous VMCM-48. Applied Catalysis A, General, 2004, 276 (1–2): 257–265